

ABSTRACT

MCGLADE, JOHN EDWARD. Directed Self Assembly of Nanospheres for NanoLithography and Nanostructured Surface Plasmon Sensors. (Under the direction of John F. Muth.)

There is substantial interest in the development of new diagnostic tools for biomedical applications. With these tools biologists will be able to develop better ideas of how individual cells function at the system level. The interactions of individual cells with the substrate upon which they reside, how cells move, and how they reproduce on the substrate are especially interesting areas. Cell mobility also appears to be different in cancerous and non-cancerous cells. As a step towards a smart microscope slide, nano-lights can be used to optically probe individual cells. This thesis focuses on the development of inexpensive nanopatterning techniques to produce arrays of nano-holes where the dimensions are substantially less than the wavelength of the interrogating light. The use of these arrayed subwavelength apertures (typically ~200 nm in diameter) allows one to exploit surface plasmon resonance effects because the distances between array elements are less than the decay length of the propagating surface plasmon. The resonant nature of the surface plasmon which can be modified by the size and periodicity of the array allows extra degrees of freedom with which to design biomolecular sensors.

A principle challenge of this work was to develop an inexpensive method where patterned structures can be produced on several different length scales. Confluent monolayers of cells are grown on cover slips or microscope slides of centimeter areas. The 10-100 μm scale sensing areas are where individual cells can be seeded and observed. Nanoholes of 100-400 nanometer diameters with 200-600 nm periodicity form arrays of subwavelength apertures within the micron scale features. These patterns can be produced using electron beam lithography or focused ion beam milling, but these methods are expensive and time consuming. In this thesis, the alternative technique of natural or nanosphere lithography is investigated. By arranging polystyrene spheres on the substrate in a two dimensional crystal. This allows the formation of a physical mask that can be used to form the array of nanoapertures.

A key feature of the work performed in the thesis is the development of techniques that combine the placement of the individual drop containing the nanospheres, and then dragging the drop in a controlled manner. This allows the uniform deposition of the nanospheres into a crystalline structure by providing a balance between the forces of evaporation and surface

tension. The periodicity of the array is determined by size of the spheres. The size of the holes can be tailored by reactive ion etching. Furthermore, by patterning the substrate on the 10-100 micron scale using photolithography it was found that within the defined areas that very good crystals without defects could be formed. This allowed meeting the goal of defining micron scale arrays, while obtaining nanoscale patterns within the defined areas. Focused ion beam milling was also used produce suitable subwavelength aperture arrays and their optical properties were investigated.

Directed Self Assembly of Nanospheres for NanoLithography
and Nanostructured Surface Plasmon Sensors

by

John E. McGlade

A thesis submitted to the Graduate Faculty of
North Carolina State University
In partial fulfillment of the
Requirements for the degree of
Masters of Science

Biomedical Engineering

Raleigh, North Carolina

December, 2007

Approved by:

Professor John F. Muth
Committee Chair

Professor David L. Lalush

Professor Orlin D. Velev

BIOGRAPHY

John McGlade was raised in West Chester, Pennsylvania by his parents Robert and Joanne. He earned his Bachelors of Science degree in Electrical Engineering from The Pennsylvania State University in 2005. While at Penn State, he worked as an undergraduate research assistant in the Communications and Space Sciences Laboratory. His interests in Biology and Optics led him to pursue the field of Optical Imaging at the Joint Department of Biomedical Engineering of UNC and NC State University. He is now completing his Masters of Science degree in Biomedical Engineering. His personality, intellect, and interests have been shaped by the exceptional people he has had the good fortune to know. This includes all of his friends, family, advisors, and coworkers.

TABLE OF CONTENTS

LIST OF FIGURES	iv
LIST OF TABLES	vi
CHAPTER 1 – INTRODUCTION	1
1.1. MOTIVATION	1
1.2. THESIS OVERVIEW	3
CHAPTER 2 – SURFACE PLASMONS	5
2.1. BACKGROUND THEORY	5
2.1.1. Maxwell’s Equations & Boundary Conditions	5
2.1.2. Conductive and Dielectric Media	7
2.2. SURFACE PLASMONS	9
2.2.1. Volume Plasmons and Surface Plasmons	10
2.2.2. Optical Excitation of Surface Plasmons	11
2.2.2.1. Propagating Surface Plasmons	11
2.2.2.2. Localized Surface Plasmons	14
2.2.3. Fabricating Plasmonic Structures	15
2.2.4. Diffraction & Scattering Effects	19
2.2.5. Optical Tuning	23
2.3. SURFACE PLASMON RESONANCE IN BIOLOGY	25
2.3.1. Biochemical Sensing	25
2.3.2. Cell/Surface Interactions	26
2.3.3. Cellular Microscopy	27
2.4. APPLICATIONS IN CANCER RESEARCH	28
CHAPTER 3 – MATERIALS AND METHODS	29
3.1. MATERIALS	30
3.2. SELF-ASSEMBLY EXPERIMENTS	32
3.2.1. Drop Coat Method	34
3.2.2. Spin-Coat Method	36
3.2.3. Directed Self-Assembly	38
3.3. MODIFIED NANOSPHERE LITHOGRAPHY	40
3.3.1. Processing Techniques	40
3.3.2. Reactive Ion Etching	43
3.4. FOCUSED ION BEAM LITHOGRAPHY	44
3.5. FABRICATION & ANALYTICAL EQUIPMENT	45
CHAPTER 4 – RESULTS AND DISCUSSION	46
4.1. PATTERNS IN SELF-ASSEMBLY	46
4.1.1. Drop-coat and Spin-coat	46
4.1.2. Directed Self-Assembly	49
4.2. FABRICATED PLASMONIC STRUCTURES	51
4.3. TUNABLE TRANSMISSION SPECTRA	58
4.4. SENSING AND IMAGING POTENTIAL	63
CHAPTER 5 - CONCLUSION	65
5.1. DIRECTED SELF-ASSEMBLY	65
5.2. NSL IN PRODUCING SUB-WAVELENGTH APERTURES	65
5.3. SUGGESTIONS FOR FUTURE WORK	66
CHAPTER 6 - REFERENCES	67

LIST OF FIGURES

Figure 1: Traditional SPR sensing	2
Figure 2: Energy gap for different material.....	7
Figure 3: Volume plasmons	10
Figure 4: Dispersion Relation	13
Figure 5: Kretschmann and Otto configurations.....	13
Figure 6: Reflectance Curve	14
Figure 7: Focused Ion Beam System	16
Figure 8: Electron Beam Lithography	17
Figure 9: Nanosphere Lithography	18
Figure 10: Transmission Intensity of Thin Gold Films	19
Figure 11: Scattered and transmitted electric and magnetic fields.....	21
Figure 12: Mie efficiency factors	22
Figure 13: Dipole Approximation of metallic nanoparticles.....	23
Figure 14: Plasmon based cell surface sensing.....	26
Figure 15: Bulls-eye pattern of a single hole surrounded by periodic corrugations.....	28
Figure 16: Forces driving self-assembly of nanospheres.....	33
Figure 17: Angled Drop-Coat Images	35
Figure 18: Angled Drop-Coat Diagram	35
Figure 19: Drop-Coat with Grid Templating.....	35
Figure 20: Spin-Coating Diagram	37
Figure 21: Spin-Coating Images.....	37
Figure 22: Spin-Coating Pillars.....	37
Figure 23: Nanoarrayer tool for Directed Self-Assembly	38
Figure 24: Silicon Nitride edge for Directed Self-Assembly.....	39
Figure 25: Packing Defects Image.....	41
Figure 26: Pre-patterned Substrate	41
Figure 27: Photoresist to protect the substrate surface.....	41
Figure 28: Modified NSL flow diagram.....	42
Figure 29: Focused Ion Beam milled periodic particles and holes	44
Figure 30: Spin-Coating 500 nm spheres at 600 rpm's	47
Figure 31: Spin-Coating 500 nm spheres at 460 rpm's	47
Figure 32: Spin-Coating 500 nm spheres at 400 rpm's	47
Figure 33: Spin-Coating 780 nm spheres at 2000 rpm's	47
Figure 34: Spin-Coating 780 nm spheres at 1000 rpm's	48
Figure 35: Spin-Coating 780 nm spheres at 250 rpm's	48
Figure 36: Spin-Coating 1000 nm spheres at 600 rpm's	48
Figure 37: Spin-Coating 1000 nm spheres at 500 rpm's	48
Figure 38: Spin-Coating 1000 nm spheres at 400 rpm's	48
Figure 39: Spin-Coating 1000 nm spheres at 300 rpm's	48
Figure 40: Dragging the meniscus at various speeds	50
Figure 41: Directed Self-Assembly shows a hard edge can be made with a straight meniscus.....	50
Figure 42: A Double layer formed from a high step height and slow dragging speed.....	50
Figure 43: Evaporation channels created via Photolithography	52
Figure 44: A 100 um square in a pre-patterned substrate	52
Figure 45: Photolithography step height and alignment.....	52
Figure 46: Unetched 1 um spheres	54
Figure 47: Etched (1:30) reduces spheres to 950nm	54
Figure 48: Unetched 1 um spheres	54
Figure 49: Etch (2:00) reduces spheres to 850nm.....	54
Figure 50: Unetched 1 um spheres	54
Figure 51: Etch (2:30) reduces spheres to 800nm.....	54
Figure 52: Unetched 1 um spheres	54
Figure 53: Etch (3:00) reduces spheres to 650nm.....	54
Figure 54: Unetched 780 nm spheres	55
Figure 55: Etch (1:30) reduces spheres to 600nm.....	55

Figure 56: Unetched 780 nm spheres	55
Figure 57: Etch (2:00) reduces spheres to 400nm	55
Figure 58: Image of 1 μm polystyrene spheres after overexposure to RIE	55
Figure 59: AFM image of holes fabricated by Nanosphere Lithography	56
Figure 60: AFM image of holes fabricated by Focused Ion Beam Milling.	56
Figure 61: Focused Ion Beam 500 nm holes	57
Figure 62: SEM after Chemical Liftoff.....	57
Figure 63: SEM after Modified NSL.....	57
Figure 64: Focus Ion Beam hexagonal apertures.....	58
Figure 65: Scattering order for a hexagonal lattice.	59
Figure 66: SEM image of Reactive Ion Etched 500 nm spheres	61
Figure 67: Hexagonal apertures	61
Figure 68: Transmission of light through structures fabricated by FIB and NSL	61
Figure 69: Polarization Dependence of transmission through honeycomb array	62
Figure 70: Transmission sensing data from periodic triangular particles	64
Figure 71: Transmission sensing data from honecomb holes	64

LIST OF TABLES

Table 1: Scattering efficiency values in differently sized gold particles.....	24
Table 2: Polystyrene spheres	30
Table 3: Particle area for sphere solution of 1% weight by volume.....	31
Table 4: Spin-coating RPM's.....	36
Table 5: Reactive Ion Etching exposure times	43
Table 6: Transmission equations for square and triangular periodic apertures.	59

Chapter 1

Introduction

1.1. Motivation

Microbiology studies are often hindered by the tradeoff between resolution and live imaging. The electron microscope offers high resolution owing to its reduced diffraction limit, but studies are performed under vacuum conditions and unsuitable for live cell studies. Real-time cellular microscopy studies have been spurred on by the development the confocal microscope and a method of synthesizing Green Fluorescent Protein (GFP) tags. Fluorescence imaging has enabled in depth looks at the functions of specific proteins involved in locomotion and signal cascades, and the confocal microscope can offer 3-Dimensional imaging with a spot size as small as 1 μm . These analytical methods have become commonplace in many research labs, yet the limitations in resolution, the number of proteins that can be studied, and exposure time still limit progress.

Fluorescent protein tagging is achievable through gene splicing methods, which encodes fluorescence on desired proteins by adding the nucleotides that code for the fluorescent protein into the regular protein gene. Other fluorescent colors have also been developed besides GFP, but due to the limitations in the number of fluorescent proteins available, only a few specific proteins can be tagged in each study. Images are captured through time-lapse photography to prevent photobleaching and damage to the cell. While great images are captured in three dimensions by confocal microscopy, substantial real-time data is mostly lost in the dark.

Surface Plasmon Resonance (SPR) is a phenomenon that has been used as a biosensor for a number of years. Figure 1 illustrates the basic concept behind surface plasmon based sensing, in which a propagating evanescent wave is generated along the surface of a thin gold film. The free electrons in the metal can oscillate in resonance with the incident light wave, and this forms an evanescent electromagnetic field that extends into the immediate surroundings. By probing the surface of a thin film, changes in the dielectric constant of a material at the surface interactions can be monitored.

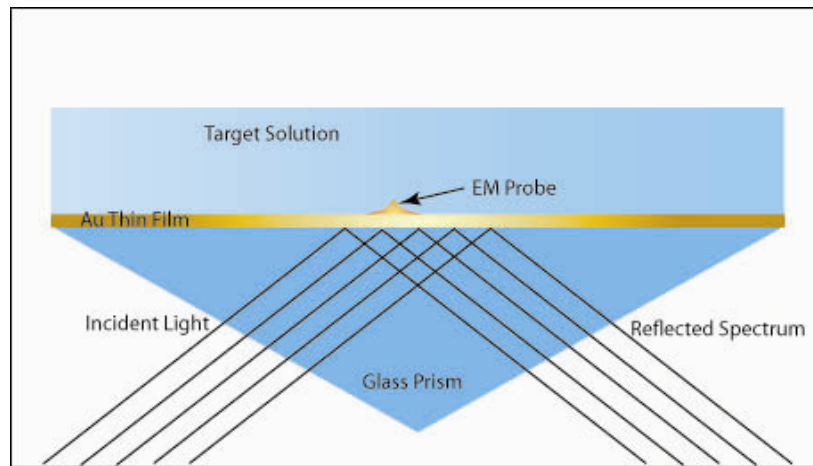


Figure 1: Traditional SPR sensing. A) A monochromatic light source is incident on the prism. The prism is rotated to sweep through a range of angles to couple the light into longitudinal electron oscillations in along thin metallic film. Instead of rotating the prism, the wavelength can be swept at a suitable angle through the visible spectrum. An intensity dip in reflection will occur at a specific wavelength.

Surface plasmon resonance was first demonstrated to have biosensing and gas detection capabilities in 1983.¹ These initial developments led the company Pharmacia Biosensor to launch the commercial BIAcore instrument for monitoring biospecific interactions in real time. Several other companies, such as Texas Instruments and Aviv, have developed commercial SPR products. SPR angle and wavelength shift detection modes are not high throughput due to the optical complexity of the instrument. More recent research in the optical properties of Localized Surface Plasmon Resonance (LSPR) suggests that they can also be used for biosensing. One advantage of LSPR are that the requirements for polarization are relaxed in comparison to Surface Plasmon Resonance in thin films. The Electric field produced by the plasmon electromagnetic wave can also be more intense, and it is localized to the particles. As in thin films, the evanescent field that interacts with the environment is typically than one wavelength in scale.

Plasmon Resonance effects can also influence light transmission through small apertures in opaque thin films. A theoretical treatment of light transmission through small holes using diffraction theory, given by Bethe,² placed a fundamental limit on the amount of light that can pass through a sub-wavelength aperture:

$$\left(\frac{r}{\lambda}\right)^4 \quad \begin{array}{l} r = \text{radius of the hole} \\ \lambda = \text{wavelength of light} \end{array}$$

However, interactions between light and plasmon resonances of periodic structures can push transmission intensity beyond this limit.³ We wish to apply the discovery of enhanced light transmission through sub-wavelength apertures⁴ to cellular biology.

Understanding proteins dynamics within the cell and the cell membrane/surface interactions can reveal the molecular mechanisms behind normal cell function and disease progression. LSPR interactions occur at ranges within the diffraction limit ($1.22\lambda/D$) and can potentially act as a near-field probe. Efforts have been made to break this barrier through sub-wavelength stimulation of fluorescent molecules,⁵ but it has been questioned as to whether these experiments really do push the limits of optical resolution into the nanometer regime.⁶ In general, obtaining quantified data at the molecular level can offer new insights into cellular biology. The use of plasmon structures shows great promise in making new tools that can potentially probe.

1.2. Thesis Overview

Experimental evidence has shown great potential for the use of Surface Plasmon Resonance in subwavelength imaging and sensing. In our research, we have modified Nanosphere Lithography to produce subwavelength apertures with a high degree of precision. This method is a high throughput alternative to expensive methods such as Focused Ion Beam or Electron Beam Lithography. The technique uses organized arrays of colloidal nanospheres to form hexagonal arrays of subwavelength holes, nanowires, or particles.

These engineered substrates could be used to selectively illuminate certain regions of a cell population, allowing for longer exposure times and reduced autofluorescence. Further research in this area could also lead to real-time, label free microscopy that operates at or within the diffraction limit. Many metals, such as silver, gold, copper, and nickel, exhibit plasmonic properties, but our project focuses on the design of plasmon structures for biological studies. Gold is relatively inert and biocompatible and has many plasmon peaks in the visible spectrum. The background and theoretical information presented in this thesis is geared towards an understanding of the mechanisms at work in thin gold films and periodic gold structures, but can be applied to silver or other plasmonic materials. A theoretical basis in electromagnetic wave theory as well as diffraction and scattering effects are presented in Chapter 2 with the scope

limited to understanding plasmonic gold structures. A review of research experiments documented by other groups and a literature review of the biological applications of surface plasmon resonance is also presented.

Experimental methods and a discussion of the results are presented in Chapters 3 and 4. Several experiments were conducted to find the best patterning method for Nanosphere Lithography, and Focused Ion Beam Lithography was also used both as a comparative tool for NSL and to explore the nature of plasmonic structures. Hexagonal spaced holes and particles can be fabricated with similar periodicities and geometry using both methods. The structures were characterized and compared with the available literature in Chapter 4. Chapter 5 includes a discussion of future work as well as the conclusion. Important equations are referenced within the text, and several mathematical derivations are included in Chapter 6 as an appendix.

Chapter 2

Surface Plasmons

2.1. Background Theory

Our experiments were aimed at fabricating nanometer scale metallic features and interrogating them with light. This section provides a theoretical background for studying the optical properties of these materials. The nature of light interacting with metal involves the transfer of electromagnetic energy between photons and collective oscillations of electrons. Photon-plasmon energy transfer depends on the electron properties of the material as well as the energy and polarization of the light source. Due to constraints of matching the wave number of the excitation with the propagating mode, only specific photon energies can be absorbed by a material. This results in characteristic absorption, reflection, and transmission bands for each material. Nanometer-sized materials differ from their bulk counterparts due to Mie scattering, which is considered in section 2.2.4.

2.1.1. Maxwell's Equations & Boundary Conditions

Maxwell's equations and the constitutive relations are the rules that govern electromagnetic fields propagating through matter. It is interesting to note that at the time of Maxwell it was not yet known that charge flow is quantized in elementary units known as electrons.⁷ Thus, the grain structure of thin films and quantum effects are ignored in a macroscopic treatment of continuous media. When the wavelength of incident light is much larger than the feature size ($\lambda \gg a$), the discrete nature of atoms and electrons are spatially averaged and usually considered homogenous.

Maxwell's equations are first-order differential equations that describe electromagnetic effects based on the spatial parameters and permittivity of the object. The constitutive relations determine the electric and magnetic flux that results from an imposed electromagnetic field and the material's susceptibility to electric and magnetic polarization.

$$\nabla \times E = -\frac{\partial B}{\partial t} \quad (1)$$

$$\nabla \times H = J + \frac{\partial D}{\partial t} \quad (2)$$

$$\nabla \cdot B = 0 \quad (3)$$

$$\nabla \cdot D = \rho_v \quad (4)$$

$$D = \epsilon_0 E + P(E) \quad (5)$$

$$B = \mu_0 H + M(H) \quad (6)$$

From these equations, one can derive the wave equation for an electric field propagating in different media. The boundary conditions at an interface between two homogenous materials can also be determined. The solution set at any interface requires that the tangential electric field be continuous and the normal electric field discontinuity be equal to the surface charge density. The tangential magnetic field is equal to the surface current J, and the normal magnetic component is continuous across the boundary.

Surface Plasmons are a Transverse Magnetic polarized waves that propagate at the interface between a metal and a dielectric. For a TM mode, only E_x , H_y , and E_z exist. In mathematical form, the electric and mathematical field equations can be described in the dielectric and metal as:

$$z < 0 \quad H_d = H_{yd} e^{i(k_{xd}x + k_{zd}z - \omega t)} \quad (7)$$

$$E_d = (E_{xd} + E_{zd}) e^{i(k_{xd}x + k_{zd}z - \omega t)} \quad (8)$$

$$z > 0 \quad H_m = H_{ym} e^{i(k_{xm}x + k_{zm}z - \omega t)} \quad (9)$$

$$E_m = (E_{xm} + E_{zm}) e^{i(k_{xm}x + k_{zm}z - \omega t)} \quad (10)$$

A propagating mode exists in the x direction, while an evanescent field exists above and below the interface. According to the boundary conditions, the tangential electric and magnetic fields must be continuous, and z components must be equal:

$$E_{xd} = E_{xm} \quad (11)$$

$$H_{yd} = H_{ym} \quad (12)$$

$$\epsilon_d E_{zd} = \epsilon_m E_{zm} \quad (13)$$

2.1.2. Conductive and Dielectric Media

The practical difference between conductors, semiconductors, and insulators is the energy gap between the valence band and the conductive band. In metals, the free electrons in the conduction band are usually considered as a gas and respond to the incident electromagnetic field. For dielectric materials there are no conduction electrons available for absorption. They can support electromagnetic fields and are often considered to have only a real dielectric constant. This concept is illustrated graphically in Figure 2.

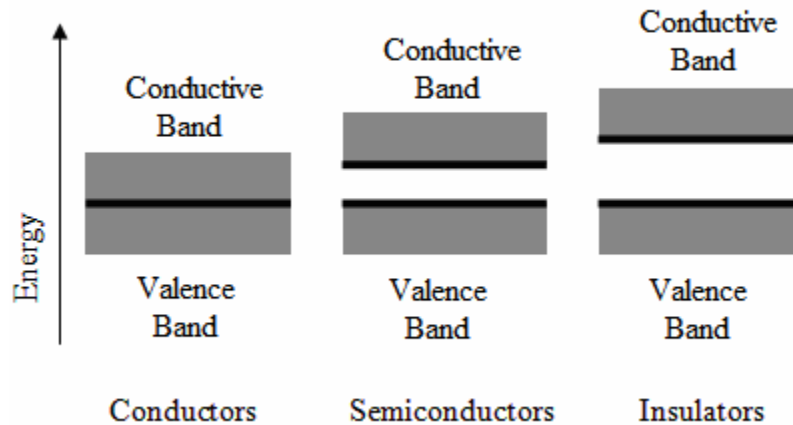


Figure 2: Energy gap between the conductive and valence bands of different material types.

In dielectric materials such as air or glass, light can travel without significant attenuation. As light passes through a material, the electromagnetic fields produce a polarization of the electron cloud around the atoms. In a dielectric, this effect on the whole material is seen as the index of refraction, $n = \sqrt{\epsilon}$, with n acting as a proportionality constant that relates the velocity of light in

vacuum to that in the material.⁸ Insulators do not absorb very much of this lossless electromagnetic energy as it passes.

In a perfect conductor, the electrons would suffer no lattice collisions and thus all of the energy would be re-radiated. They would also oscillate simultaneously with a driving electromagnetic field because there would be no restoring force and no natural frequencies. A perfect conductor is an idealized material in which no electric field is allowed to exist. Electric fields cannot exist within the interior because the fields are screened by currents on a conductor's surface.

The optical properties of real metals can be explained by a plasma model. Electrons oscillate in response to an electromagnetic field, and losses arise out of electron collisions with the positive lattice background or with crystalline imperfections and convert electromagnetic energy into heat. When described as a damped harmonic oscillator with a collision frequency, $\gamma = \frac{1}{\tau}$, the dielectric function can be written as a function of the driving frequency and material constants of the metal (ω_p and γ):

$$\varepsilon(\omega) = 1 - \frac{\omega_p^2}{\omega^2 + i\gamma\omega} \quad (14)$$

This term can be separated into a complex number, in which the imaginary component describes the damping associated with absorption of light in conductive material.

$$\varepsilon(\omega) = \varepsilon_1(\omega) + i\varepsilon_2(\omega) \quad (15)$$

The absorption of radiant energy varies according to its free-electron charge density and the mobility of the electrons in the metal. Furthermore, there is a frequency response to an applied electric field due to the finite time required to induce polarization.⁹ When the permittivity or permeability is a function of the frequency, we call the medium dispersive.

Free conduction electrons have no natural frequencies, while bounded electrons will have driving frequencies. The dielectric constant of every material exhibits frequency dependence. As light passes from a vacuum into a material body, the speed of light is reduced by a factor that is the reciprocal of the refractive index, where the refractive index in a non-absorptive material is the square root of the dielectric constant.

$$c = \frac{c_0}{n} = \frac{c_0}{\sqrt{\varepsilon}} \quad (16)$$

Energy conservation implies that the frequency of light is constant, regardless of the medium. This requires the refractive index of a medium to increase and the wavelength to decrease. Thus, for a defined length of material, the optical phase varies more rapidly.

Surface Plasmon Resonance requires an interface between a metallic film and a dielectric. The permittivities of these materials are of opposite sign and establish an optical waveguide. The dielectric constant of a material describes its ability to be polarized by electromagnetic waves, but conduction electrons and screening effects prevent this from occurring in metals. In lossy metals the constant becomes a complex number to describe the damping factor. A negative permittivity is necessary in establishing Surface Plasmon Polaritons

2.2. Surface Plasmons

Standard optics for metals, semiconductors, and insulators is based on the assumption that only transverse electromagnetic plane waves propagate in the material. In metals, the motions of electrons are modeled as free particles with a background potential, this is known as the Drude Model. At certain frequencies, coulomb interactions between electrons of metals result in charge density buildups, which are the longitudinal plasma waves first discovered in the 1950's.¹⁰ It became apparent at that time that plasma waves should be included in metal optics¹¹ because of deviation from the Fresnel equations¹² that results in diminished reflectivity when plasma waves are excited. Increasingly conductive metals have sharper resonance peaks because of less damping. Metals that show particularly strong plasmon peaks are the noble metals (Cu, Au, Ag). Optical absorption occurs at depths as far as several hundred angstroms, but the electrons excited near the surface have a higher probability of contributing to photoemission. Thus, for optical devices, thin layers of noble metals can be engineered to display interesting optical properties.

2.2.1. Volume Plasmons and Surface Plasmons

Both volume and surface plasmons can be excited optically,¹³ and these waves were first detected in 1970.^{14, 15} However, the probability of exciting volume plasmons with photons is small for visible light due to short penetration depths of metals, and particle excitation is instead used. In electron loss spectroscopy experiments, fast moving electrons are driven into thin metallic films. A space charge of finite density can build up, and the gradient of the electron density causes restoring forces to push the metal electrons along the z direction according to the frequency of the light. These are longitudinal density oscillations of the electrons, or volume plasmons, as illustrated in Figure 3.

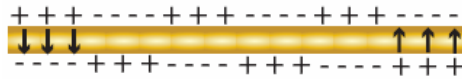


Figure 3: Volume plasmons are longitudinal electron density fluctuations in a metal film.

For bulk (or volume) plasmons, the plasma frequency oscillates according to the free electron density and effective mass. When the frequency of excitation ω is greater than the plasma frequency,

$$\omega_p^2 = \frac{4\pi n e^2}{m_e} \quad (17)$$

the metal becomes transparent. At frequencies lower than the plasma frequency, a propagating transverse electromagnetic wave is forbidden and an evanescent wave is generated. In this expression, n is the volume electron density, e is the electron charge, and m_e is the mass of electrons.

Surface plasmons behave differently than volume plasmons due to imposed boundary conditions at the interface. A polariton is a coupling between a photon and an electron. Surface Plasmon Polaritons are transverse electromagnetic wave coupled to oscillating electrons at the surface of a metal. Using the Maxwell's curl equation for H in both mediums, the condition for Surface Plasmon coupling can be found:

$$\frac{k_{zm}}{\epsilon_m} = \frac{k_{zd}}{\epsilon_d} \quad (18)$$

When incident light strikes the boundary of a solid at an angle θ against the normal, it has an E component normal to the surface (z direction). The electromagnetic fields are at a maximum at the interface, and decay exponentially away from the surface (z direction). The surface waves are by their very nature polarized propagating light, so they must be excited by Transverse Magnetic waves, or p -polarized light. In the case of light incident at an angle, s -polarized light means that the E vector is parallel to the plane of incidence, while p -polarized light is perpendicular.

2.2.2. Optical Excitation of Surface Plasmons

Surface Plasmon Polaritons were first observed in fast electron energy loss experiments and later by losses in optical reflection intensity. Plasmons can be excited optically on planar surface or in confined spaces on the order of the wavelength of incident light. Planar surfaces provide translational invariance that allow for propagating surface plasmon modes. Propagating modes are characterized by their propagation distance along the surface, the penetration into the surrounding medium, and the penetration depth into the metal.

2.2.2.1. Propagating Surface Plasmons

The first experimental observation of light excitation of a metal surface was made by Wood.¹⁶ In his experiments, white light passed through a metallic grating and a significant amount of light absorption was observed for certain frequencies, as evident from the diffraction pattern. He also noted the polarization dependence of transmitted light. “Polarization proved to be the key to the explanation of the very singular behavior of the grating of which I am writing. Experiment proved this to be the case, for it was found that the singular anomalies were exhibited only when the direction of vibration was at right angles to the ruling.” The light was coupled to the surface when the E -field had a perpendicular polarization to the metallic edges. This is an example of using a grating to generate surface plasmon waves.

Surface plasmon polaritons occur at the interface between a metal and a dielectric material in which the real part of dielectric constant less than zero. There are two methods of generating addition momentum for surface plasmon polariton coupling: attenuated total reflection or through grating couplers. Wood illustrated one method of generating surface plasmon

absorption, through a grating coupler. Another method of doing so is through attenuated total internal reflection. Attenuated total reflection (ATR) provides the external radiation with an imaginary wave vector in the direction perpendicular to the surface.

Surface plasmon resonance is a momentum coupling between the electrons at the surface of a metal and the incident light. Coupling light to the metallic surface at certain frequencies gives rise to a partial absorption of that radiation. The wave-particle duality allows us to examine the wavelengths associated with photons and electrons as described by the de Broglie postulate. The de Broglie relations state that the wavelength of light is inversely proportional to the momentum of a particle (Eq. 19). Since the momentum is proportional to the mass of a particle, the wavelengths associated with electrons are considerably shorter than photons. When the momentum of the photons and electrons are matched, electromagnetic coupling can occur.

Fundamental to understanding Surface Plasmon Resonance is the dispersion relation, which states that the medium of travel directly determines the momentum of the wave (Eq. 20). The wave number for light propagating in a dielectric material and the surface plasmon wave along the boundary of a metal and dielectric are defined by the real part of the dielectric constants at the boundary (21a & 22b).

$$\lambda = \frac{h}{p} \quad (19)$$

$$k^2 = \omega^2 \mu_0 \epsilon \quad (20)$$

$$k_{\text{vacuum}} = \frac{\omega}{c} \sqrt{\epsilon_d} \quad (21)$$

$$k_{sp} = \frac{\omega}{c} \sqrt{\frac{\epsilon_m \epsilon_d}{\epsilon_m + \epsilon_d}} \quad (22)$$

A graph of equations 21 and 22 in Figure 4 show that the wave number for the surface plasmon wave approaches the light line at small k , but they do not intersect for vacuum or air. At a given photon energy, the wave vector has to be increased by a certain value in order for the electrons to absorb the photons. The reason that these lines never cross is due to the fact that the real part of the dielectric constant of a metal is always less than -1. The resulting plasmon curve becomes an increasing quadratic function that approaches 1 at infinity. Plasmon coupling is possible by slowing the momentum of the incident light wave. This is achieved using materials with higher refractive index.

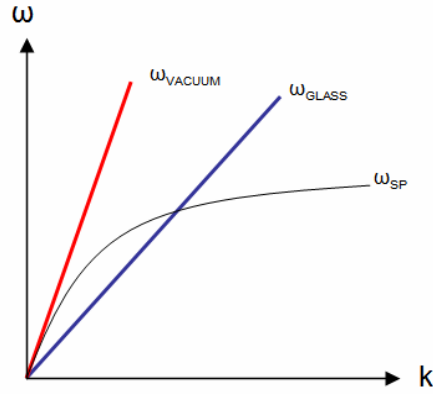


Figure 4: Dispersion relation shows a momentum mismatch between incident light and surface plasmons at the boundary of a metal/air interface. This can be overcome through the use of a glass prism.

Kretschmann and Otto proposed ways of exciting the surface plasmons optically by using a high index prism in an attenuated total reflection configuration, as illustrated in Figure 5. When light strikes a prism, it is split into its wavelength components due to chromatic aberration. The ingenuity of this approach is to analyze the k vector by Cartesian coordinates. When light strikes an interface at an angle to the normal, the electric and magnetic waves can be described in terms of a magnitude and a momentum vector:

$$k = \hat{x}k_x + \hat{y}k_y + \hat{z}k_z \quad (23)$$

Under the total internal reflection condition, a propagating wave is generated along the interface of the prism. The continuity equations now factor in with matching electric fields in the x direction on both sides of an interface, and matching magnetic fields in the y direction. These conditions establish an evanescent wave that decays exponentially to the surface normal (z direction).

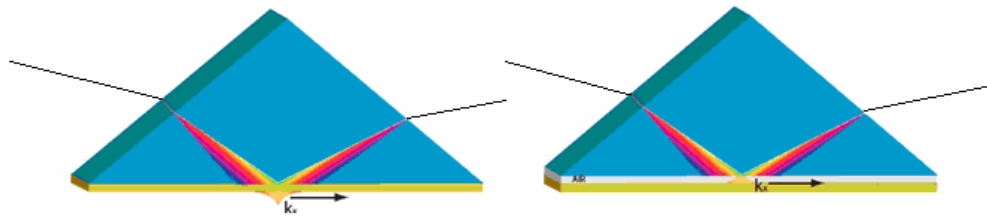


Figure 5: Kretschmann and Otto configurations for optically exciting surface plasmons. Kretschmann used a thin film deposited directly onto the prism, while Otto allowed a small air gap between the prism and a thin gold film.

By sweeping the incident light through different angles of incidence, an evanescent wave can be generated, as described by the following equation:

$$k_{evanescent} = \frac{\omega}{c} \sqrt{\epsilon_{glass}} \sin \theta \quad (24)$$

At a certain angle beyond total internal reflection, an evanescent wave can couple into a propagating surface plasmon wave. This coupling can be observed as a dip in the reflection intensity (Figure 6).

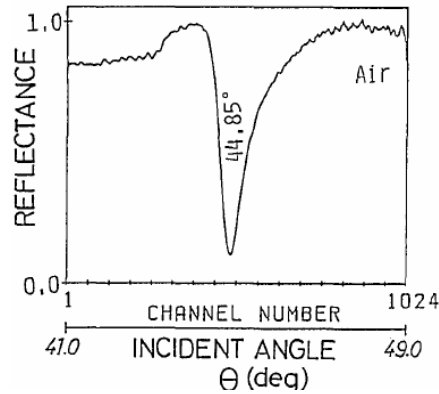


Figure 6: Reflectance curve of a thin film in the Kretschmann configuration, reproduced from [17].

2.2.2.2. Localized Surface Plasmons

Attenuated Total Reflection as a method of generating surface plasmon waves is difficult to set-up experimentally, and the detailed spatial resolution is limited. Localized Surface Plasmons can be generated for normally incident light for materials with limited spatial dimension. The momentum matching conditions necessary for generating propagating Localized Surface Plasmons are generated due to random scattering events at a roughened surface. For example, shining light into a solution of colloidal metal spheres generates random scattering in which a certain portion of the light is incident at the resonance angle. Fixed particles and films with constrained dimensions can also generate Localized Surface Plasmon modes. These effects are determined by the periodicity of the structures. Scattering events can be treated by a variety of modeling techniques, which will be discussed in section 2.4.

2.2.3. Fabricating Plasmonic Structures

Metallic nanostructures can be generated in suspension or on the surface of a substrate. Suspended nanoparticles are fabricated by chemical reduction of metal salts in the presence of a surfactant or template. This can also be used as the first step in generating core-shell particles. Nanostructures on a substrate surface are created by a combination of lithography techniques and physical methods such as metal evaporation in a vacuum.¹⁸ This section explores three of the many surface fabrication techniques that can produce surface-bound plasmonic structures: Focused Ion Beam Lithography, Electron Beam Lithography, and Nanosphere Lithography. Our lab group has employed Nanosphere Lithography and Focused Ion Beam lithography in our experiments, and Electron Beam Lithography is described due to its established potential. Other emerging nanolithographic techniques include nanoimprinting methods such as Dip-Pen Lithography and Imprint Lithography as well scanning probe-based methods, but they are omitted in this review.

Electron beam lithography has been the standard approach to making nanostructures, in which a thin layer of photo-resist is exposed to electrons, and then a chemical development is performed. Focused Ion Beam lithography is a recently developed method of creating various patterns on-the-fly. Both Electron beam lithography and FIB lithography are expensive, serial methods. A parallel processing method is to use colloidal particles as deposition and etch masks in Nanosphere Lithography.

Focused Ion Beam

A Focused Ion Beam can be scanned along the sample to either sputter atoms from the surface or cause decomposition of an organic vapor on the surface of the substrate (subtractive or additive lithography). A liquid metal ion source is used to generate a stream of ions that are accelerated to tens of kilo electron volts and focused onto the target surface using electrostatic lenses. The beam current and exposure time can be optimized for each material and thickness, but charging effects on insulating materials can sometimes cause the beam to drift. Gallium is the typical metal because it is liquid near room temperature. Focused Ion Beam can sculpt features of any specification. Features such as slits, isolated particles, and even 3-Dimensional shapes can be fabricated. The surface is modified point-by-point, which is a slow process. A computer interface (Figure 7) allows the user to specify the exact features. Many of the studies produce a square array of holes and ellipses for ease in mathematical analysis.

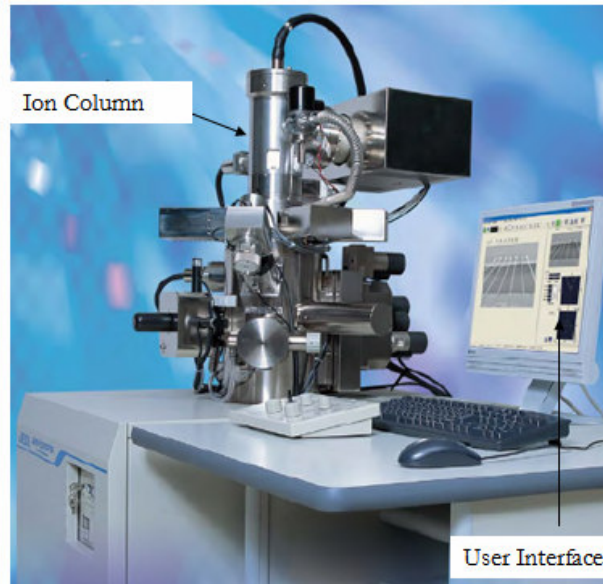


Figure 7: Typical Focused Ion Beam System. User interface and Ion column are indicated. Image reproduced from JEM-9320 FIB manual.

Electron Beam Lithography

Writing with electron beams to produce small features has been used for a long time and is based on the technology developed for Scanning Electron Microscopy. The beam diameter is about 10 nm, and the intensity profile is a Gaussian beam. They are focused by a series of magnetic lenses and apertures. The systems also use electrostatic plates or magnetic deflection coils to deflect the beam and correct for astigmatism. One deflector within the electron column is used to blank the beam on and off at the appropriate times while a second deflector is used to scan the beam across the sample.

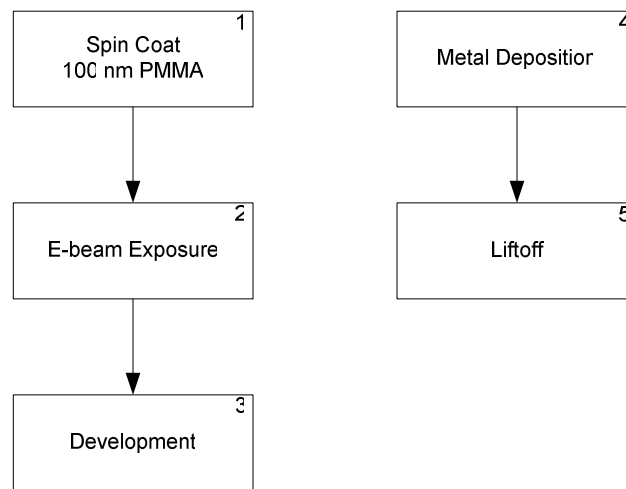


Figure 8: Fabrication process in Electron Beam Lithography.

Electron beam scanning is limited to small distances due to aberrations and distortions introduced by the deflection fields. The general idea of decreasing wavelength and increasing numerical aperture has proved successful but at the cost of decreased depth of focus (DOF):

$$DOF = \pm \frac{0.5\lambda}{(NA)^2} \quad (25)$$

More stringent requirements on planarity and wafer flatness are necessary, leading to nanometer scale flatness necessary for substrate exposure.¹⁹ Still, the major drawback of e-beam lithography is the serial nature of feature production.

Nanosphere Lithography

Nanosphere Lithography uses colloidal spheres, usually polystyrene or silica, as a deposition or etch mask. Colloidal dispersions are usually prepared by emulsion polymerization,²⁰ and colloidal spheres can be used for a wide variety of applications.²¹ Polystyrene spheres are usually synthesized in the presence of surfactants, but surfactant-free polystyrene spheres have also been synthesized.²² They were first used as a deposition and etch mask in a process referred to as natural lithography,²³⁻²⁵ and they can also be used directly as a lithographic mask.²⁶ Nanosphere Lithography is the more recent term used to describe the use of natural lithography in fabricating materials with engineered optical properties. The term was coined by R. P. Van Duyne's research group, in which they characterized the optical filtering properties of Ag nanoparticles on mica substrates.^{27,28} Since that time, a variety of structures have been fabricated using angular deposition²⁹ or by modifying the process to obtain rings, pillars, and spikes.^{30,31} Double-layer crystals can also be formed through self-assembly in a pattern of either farther spaced hexagonal arrays or in a square lattice structure.³² Randomly dispersed spheres generated through NSL can also be useful for fabrication of nanoholes of various diameters in optically thin films.³³ Figure 9 illustrates the major steps of Nanosphere Lithography: the self-assembly of spheres, a metallic deposition, and a liftoff. Several variations can be applied to this method to achieve a different metallic thickness and periodicity.

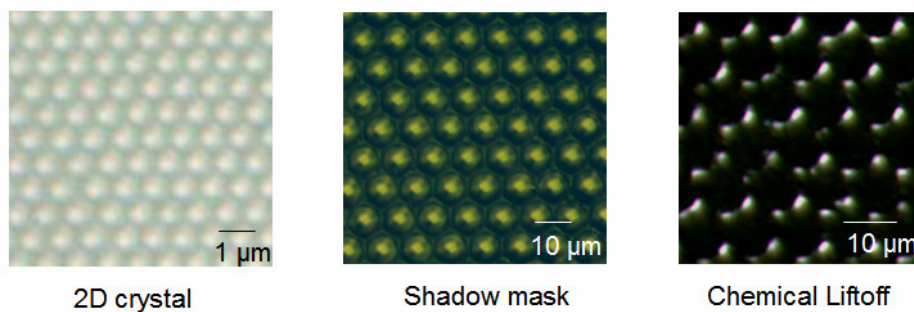


Figure 9: Steps involved in Nanosphere Lithography. A) Assembly of a 2-dimensional crystal of spheres, B) Spheres are used as a deposition mask for a metallic layer, C) Periodic patterns are revealed after a chemical liftoff using dichloromethane.

2.2.4. Diffraction & Scattering Effects

Much of the past experimental data for simple metals apply the Drude model, which treat the electrons as nearly free but experiencing some collisions. The Drude model is a reasonable basis for predicting the classical optical properties of metals at frequencies below the threshold for interband transitions. The Drude model describes the conduction of free electrons as having a damping force proportional and opposite in direction to the motion of the electrons. The plasma frequency depends on the average density of conduction electrons, the mean scattering rate for these electrons, and the core polarizability of the ions.³⁴

When the film is made extremely thin, the optical response of noble metals is further complicated by interband transitions. At energies above the Fermi band, photons can be absorbed and re-emitted. Figure 10 shows the relative transmission of light in samples between 25 nm and 100 nm in thickness. There is an intense drop-off of transmitted light after the penetration depth is exceeded by several orders.

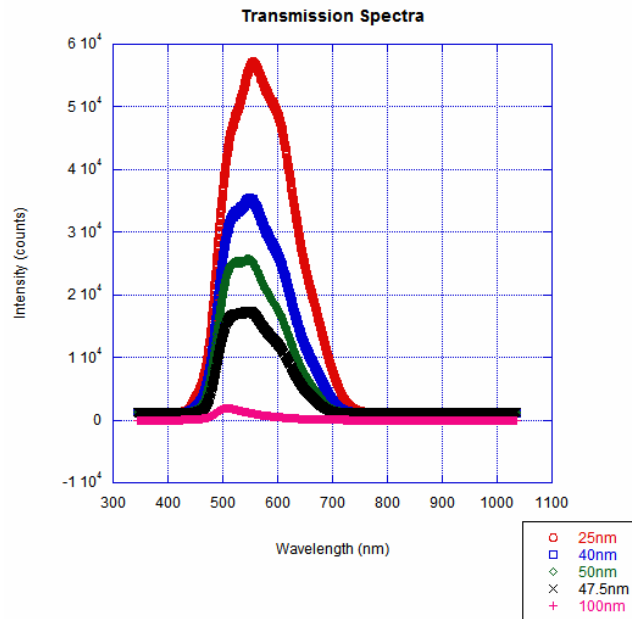


Figure 10: Increasing thickness in gold films show the rapid drop-off in transmission intensity for beyond 50nm. The green plot (♦) shows the drastic change when a thin layer of chromium (2.5nm) is introduced for better surface adhesion.

The Drude model for free electrons in an ion gas model has limitations in calculating the plasmonic response of noble metals due to absorption from interband transitions from the outermost d orbital to the next sp orbital at visible and ultraviolet frequencies.³⁵ Therefore, a modification is made to account for this susceptibility.

$$\varepsilon(\omega) = \left(1 - \frac{\omega_p^2}{\omega^2 + i\omega\gamma_{bulk}} \right) + \varepsilon(\omega)_{interband} \quad (26)$$

1st term = Drude free electron
 ω_p = bulk plasmon frequency
 γ_{bulk} = bulk collision frequency
 $\varepsilon(\omega)_{interband}$ = interband trans.

Interband transitions are an additional electric susceptibility that changes the dielectric constant, $\varepsilon(\omega)$. Noble metals have incomplete bound electron shells, and variations in the configuration of these shells allow for low-energy excitation by optical (Au, Cu) and infrared light (Ag). If a metal has a particular color, it indicates that the atoms are partaking of selective absorption by way of the bound electrons, in addition to the general absorption characteristic of the free electrons. In gold, the outermost (6s) shell and the next-inner (5p) shell has a small energy difference (1.8 eV). Alterations between the $5d^96s^2$ and $5d^{10}6s$ configuration allow gold to absorb blue light and, thus, look yellow. Silver is unable to absorb any light in the visible spectrum and appears totally reflective.

For periodic structures, such as perforated thin films and small particle arrays, the wavelength is approximately equal to the feature sizes ($\lambda \approx a$). Periodic patterns and geometries at this scale can alter the local electromagnetic fields at the interface and yield different optical effects. Consequently, the absorption and emission spectra from a small particle can have features where none exists in the bulk. The dielectric function of metal particles is dependent not only upon the frequency of incident light, but the size and shape of the small particles and the arrangement of other nearby metallic particles. By understanding diffraction and scattering theory well as additional boundary conditions to Maxwell's equations, we can better interpret the events occurring at this scale.

Scattering of electromagnetic waves were first studied over 100 years ago by Lorentz,³⁶ Mie,³⁷ and Debye.³⁸ When the radius of particle is much smaller than λ , Rayleigh scattering occurs and quasi-static calculations can be used. In other words, the spatial variation of the electromagnetic field is neglected while the temporal dependence is preserved. The limited mean free path of the electrons is the most important factor leading to modifications of the relaxation time, plasma frequency, optical constant and dielectric constant. By the increasing of

the particle diameter from $(\lambda/10) \rightarrow \lambda$, the relaxation time increases rapidly and the Rayleigh approximation can no longer be used. The structures fabricated in this work are of comparable size to the wavelengths of optical light, so Mie theory is an appropriate model to consider.

Exact solutions for the optical properties of metal nanostructures can be obtained using Mie theory, whose formulations are derived from Maxwell's equations. The scattering of light by an isolated sphere was treated with appropriate boundary conditions. Mie and Debye approached the problem of spheres suspended in a homogenous medium, where it is assumed the spheres are far enough apart that the scattering is incoherent. Mie studied the color of light scattered from an isolated sphere, while Debye considered the radiation pressure of light. The solutions are still relevant today, and they are often cited in the literature.

Application of Mie theory requires ϵ_d and $\epsilon_m(\omega)$ be specified for a given particle size, either as experimental values or as numerical approximations. Mie theory uses spherical coordinates to more easily input boundary conditions. If an electromagnetic plane wave is incident upon an isotropic sphere, there will be scattered electric and magnetic fields outside the sphere as well as transmitted fields inside the sphere (Figure 11).

$$E_{sc}(r) = \sum_{l,m} \left[\left(\frac{ic}{\hat{n}_2^2} \omega_0 \right) \beta_E(l,m) \times \nabla \times [h_1^1(k_2 r) Y(\hat{r})] + \beta_M(l,m) h_1^1(k_2 r) Y(\hat{r}) \right] \quad (27)$$

$$B_{sc}(r) = \sum_{l,m} \left[\beta_E(l,m) [h_1^1(k_2 r) Y(\hat{r})] - \left(\frac{ic}{\hat{n}_2^2} \omega_0 \right) \beta_M(l,m) \times \nabla \times [h_1^1(k_2 r) Y(\hat{r})] \right] \quad (28)$$

$$E_{tr}(r) = \sum_{l,m} \left[\left(\frac{ic}{\hat{n}_1^2} \omega_0 \right) \gamma_E(l,m) \times \nabla \times [j_1^1(k_1 r) Y(\hat{r})] + \gamma_M(l,m) j_1^1(k_1 r) Y(\hat{r}) \right] \quad (29)$$

$$B_{tr}(r) = \sum_{l,m} \left[\gamma_E(l,m) [j_1^1(k_1 r) Y(\hat{r})] - \left(\frac{ic}{\hat{n}_1^2} \omega_0 \right) \gamma_M(l,m) \times \nabla \times [j_1^1(k_1 r) Y(\hat{r})] \right] \quad (30)$$

Figure 11: Scattered and transmitted electric and magnetic fields. Reproduced from [39].

Boundary conditions are introduced by equating the tangential components of the inner and outer fields at the interface between the two media, and the solutions for the fields are expressed in a series expansion of vector eigenfunctions ($\beta_E, \gamma_E, \gamma_M$) that form a complex set. When discussing the power removed from the incident beam, efficiency factors are used. Efficiency factors are

unitless quantities that quantify the loss due to the polarization of the incident wave and the geometry of the particles. The efficiency factors for scattering, extinction, and absorption are a function of the nanoparticles cross-section and relate in the following way:

$$Q_{scattering} = \left(\frac{2}{k_2^2 a^2} \right) \sum_{l=1}^{\infty} (2l+1) \left[|\beta_E(l, m)|^2 + |\beta_M(l, m)|^2 \right] \quad (31)$$

$$Q_{extinction} = \left(\frac{2}{k_2^2 a^2} \right) \sum_{l=1}^{\infty} (2l+1) \operatorname{Re}[\beta_E(l, m) + \beta_M(l, m)] \quad (32)$$

$$Q_{absorption} = Q_{extinction} - Q_{scattering} \quad (33)$$

Figure 12: Mie efficiency factors for scattering, extinction, and absorption, are the corresponding cross sections divided by the projected area of the scattering spheres (πa^2).

The terms in the summation for $Q_{scattering}$ and $Q_{extinction}$ represent the electric and magnetic multipoles. For example, the term for $l = 1$ represents a dipole. The β terms are Bessel and Ricatti functions that depend on the index of refraction of the material. Small particles have been found to show a Mie resonance not found in bulk metal. In bulk gold, the conduction-electron mean free path at room temperature is approximately 42 nm. In the size regime below the mean free path of electrons, dipole plasmon absorption is the dominant contributor to the extinction spectra. With particle diameters greater than 50 nm, the effects are purely electromagnetic and involve contributions from higher-order multipoles. When the mean free path is satisfied, the plasmon resonance broadens as well. The solution of Mie was derived for a single sphere, and it can only be applied to many spheres if they are all of the same composition and they are randomly distributed with separation distances that are large compared to the wavelength. Our samples do not match this criteria because there is coherence in the scattered light from the periodic holes.

Approximations to Maxwell's equations are employed to solve for complex shapes. One approximation method of analysis is the dipole approximation, as illustrated in Figure 13. The oscillation of conduction electrons, driven by the electromagnetic field of light, produces oscillating dipoles along the field direction and the electrons are driven to the surface of the nanoparticles.

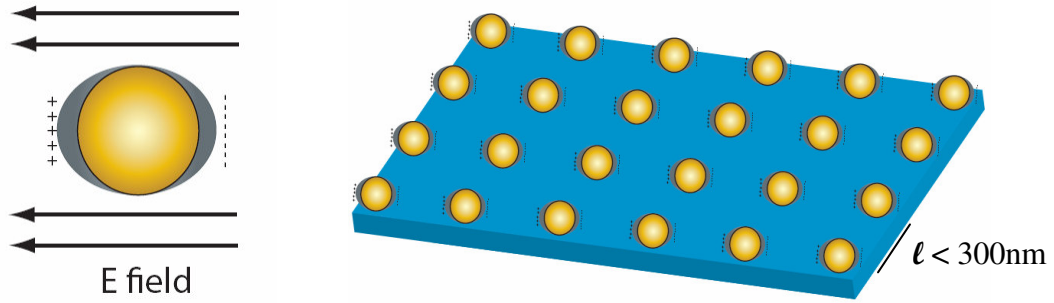


Figure 13: Dipole Approximation of a metallic nanoparticle in which electrons oscillate parallel to the electric field. The periodic arrangement causes electromagnetic coupling between the particles.

The Discrete Dipole Approximation was first proposed in the early 1970's⁴⁰ and is used by the Van Duyne group to analyze periodic nanoparticles generated through Nanosphere Lithography. It is a numerical approximation to Maxwell's equations and is used to calculate Mie efficiency factors for particles of arbitrary shape. Dipole-dipole interactions are also taken into account, which have length scales that can extend for several hundred nanometers. This method could be very useful for our structures if it is adapted to account for potential propagating modes in the veins between our apertures.

2.2.5. Optical Tuning

Interest in research and commercial applications of metallic nanostructures has coincided with advances in colloidal science, Localized Surface Plasmon Resonance (LSPR) technology,⁴¹ and Surface Enhanced Raman Spectroscopy (SERS).⁴² Noble metals (Au, Ag, Cu) have a particularly strong SERS response due to resonant optical excitations of the electrons, and the spectral characteristics correlate with shape, size and periodicity arrangements as well as the dielectric environment. Size dependence of the surface plasmon resonance comes from the size dependence of the dielectric constant, ϵ_m , of the metal.⁴³ Plasmon absorption peaks can be optimized for a number of alkali and noble metals.⁴⁴ For values of Q_{sca} greater than 1, the particle is able to scatter photons which are outside the physical cross-sectional area of the particle.

Table 1: Scattering efficiency values for the maximum peak absorption in different sized gold particles. Reproduced from [45].

Calculated Light Absorption and Scattering Properties for Gold Particles of Different Sizes							
Dia (nm)	λ_{\max} (nm) ^a	C_{sca} (cm ²)	$I_{\text{U}}(0)$	$I_{\text{U}}(90)$	ϵ (M ⁻¹ cm ⁻¹)	φ_{s}	Q_{sca}
20	535	8.36×10^{-14}	1.77	0.882	1.57×10^9	0.014	0.027
40	535	6.05×10^{-12}	129	63.9	1.63×10^{10}	0.1	0.482
60	545	6.33×10^{-11}	1.35×10^3	668	5.32×10^{10}	0.313	2.24
80	555	2.31×10^{-10}	4.97×10^3	2.44×10^3	1.14×10^{11}	0.546	4.6
100	575	4.56×10^{-10}	9.84×10^3	4.83×10^3	1.62×10^{11}	0.739	5.81
120	605	6.9×10^{-10}	1.48×10^4	7.32×10^3	2.07×10^{11}	0.876	6.1
140	635 ^b	8.79×10^{-10}	1.89×10^4	9.4×10^4	2.46×10^{11}	0.94	5.71
160	665	1.02×10^{-9}	2.22×10^4	1.11×10^4	2.8×10^{11}	0.963	5.09
180	560	1.16×10^{-9}	2.5×10^4	1.27×10^4	3.14×10^{11}	0.974	4.56
200	565	1.38×10^{-9}	7.53×10^4	1.86×10^4	4.51×10^{11}	0.788	4.39
300	565	2.94×10^{-9}	1.7×10^5	3.82×10^4	7.98×10^{11}	0.968	4.16

^a Wavelength of the maximum peak of the scattering cross section vs wavelength graph in the wavelength range 380–700 nm. Entries in all columns of the same row are for the maximum peak wavelength.

^b For diameters greater than 140 nm, two peaks appear in the light scattering spectrum. See Fig. 6b. Data are tabulated at the wavelength of the most intense peak.

Note. C_{sca} , Light-scattering cross section. $I_{\text{U}}(0)$ and $I_{\text{U}}(90)$, Scattered light intensities measured at 0 (forward) and 90° with respect to the direction of an unpolarized incident light beam. ϵ (M⁻¹ cm⁻¹), Molar decadic extinction coefficient. φ_{s} , Light-scattering yield defined by Eq. [17]. Q_{sca} , Scattering efficiency defined by Eq. [14]. Medium refractive index = 1.33.

In the case of noble metals such as gold, there are two types of contributions to the dielectric constant of the metal: One is from the inner d electrons, which describes interband transitions (from inner d orbitals to the conduction band), and the other is from the free conduction electrons. The latter contribution is described by the Drude Model,⁴⁶ which was developed to analyze simple metals.

In bulk metal, the damping constant is due to electron-electron scattering and electron-phonon scattering. This scattering produces a damping term that is inversely proportional to the particle radius r . In small nanoparticles, scattering of electrons from the particles boundaries (surfaces) also become important. The dependence of the damping term on particle size introduces the size dependence in ϵ_{m} . For larger-size nanoparticles, higher-order charge cloud distortion of conduction electrons becomes important. As the particle size increases, this has a pronounced shift of the plasmon resonance condition.

The position and shape of the plasmon absorption band depends on the dielectric constant ϵ_{d} of the surrounding medium, as the resonance condition is described by $\epsilon_{\text{m}} = -2\epsilon_{\text{d}}$. Electromagnetic field interactions between periodic and isolated particles show a high degree of sensitivity to the surrounding dielectric environment, which has found immediate application biochemical sensing⁴⁷ and have also incited interest for their potential as optical switches and waveguides.⁴⁸

2.3. Surface Plasmon Resonance in Biology

In propagating plasmon wave, the photons and electrons are completely confined to the surface, but energy can leak into the periphery by generating an evanescent wave. The field distribution in this (classically forbidden) region decays exponentially into the medium of lower refractive index from the boundary of the guiding region. In Localized Plasmon modes, the surrounding dielectric media influences the scattering of electromagnetic waves from small features. Gold thin films and particles are used most in the biological environment due to their inertness, stability, and optical properties.⁴⁹ This section discusses the applications of gold nanostructures in biological and chemical sensing.

2.3.1. Biochemical Sensing

Optical absorption in metallic nanostructures causes the surface state of the metal to be highly sensitive to adsorbed contaminants.⁵⁰ Research in this area can form a platform for new applications in chemical and biological sensing. Surface plasmon resonance spectroscopy is a useful technique for studying antibody-antigen, DNA-DNA, DNA-protein, protein-protein, and receptor-ligand interactions. This is a well established technique that uses the traditional method of Attenuated Total Reflection to excite plasmons in a continuous thin film. Typically, the penetration depth for visible light on a gold surface is between 50 and 100 nanometers. Protein adsorption and desorption studies can reveal subtle information about the conformational states of proteins that directly affect binding kinetics.⁵¹

Optical sensing can take place through direct and indirect methods. Direct biosensing measures direct antigen/antibody binding without secondary labels. Indirect sensing uses labels that are attached to the analyte of interest, such as fluorescent or luminescent molecules. One challenge in SPR sensing is in measuring dissociation rates when while high affinity interactions. However, using low affinity receptor-ligand pairs can lead to non-specific binding that corrupts the data.

SERS biosensors have been fabricated by Nanosphere Lithography,⁵² although most of the studies with metallic nanoparticles have used silver due to its sharper resonance peaks. There is a smaller body of research that uses gold particles probably because the SPP resonance has a

very broad feature in the blue/green part of the spectrum. Hence, there is a need for careful detection of the subtle resonance curve.

2.3.2. Cell/Surface Interactions

Cell/substrate focal contacts take place between membrane integrins and surface peptide sequences. They can bring the cell membrane as close as 10 nm to the substrate surface, while most of the membrane remains between 100 and 150 nm above the substrate. Measuring cell/substrate distances can be performed through interference reflection microscopy (IRM), total internal reflection fluorescence microscopy (TIRFM), and more recently, surface plasmon resonance imaging.⁵³

Several integrins are involved in focal contact formations; however, the mechanism of integrin migration and clustering at the leading edge of a mobile cell is still largely unknown. Evanescent wave excitation and surface plasmon based sensing offers promise in unraveling the mysteries of contact formation.

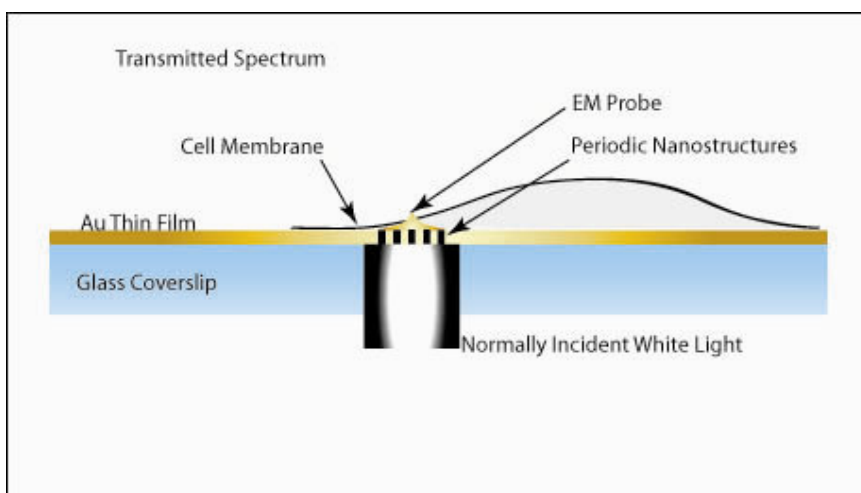


Figure 14: Plasmon based cell surface sensing using periodic nanostructures fabricated in thin gold film.

Evanescent wave excitation can also be used for fluorescence sensing with high near surface selectivity.⁵⁴ The evanescent wave energy can be absorbed by a fluorophore to generate fluorescence emission, which is then used to image fluorescently labeled biological targets. Because of the short-range exponentially decaying nature of the evanescent field, only the fluorescently labeled biological specimen near the substrate surface generates fluorescence and

can be thus imaged. This allows TIR microscopy to obtain a high quality image of the fluorescently labeled biologic material near the surface with very low background fluorescence and minimal exposure of cells to light in other planes.⁵⁵

2.3.3. Cellular Microscopy

Surface Plasmon Microscopy was first introduced in 1988 using ATR excitation of a thin gold film.⁵⁶ The scattering and surface chemistry properties of gold nanoparticles also make it an ideal candidate for cellular microscopy studies. Surface Plasmon Resonance has been used to help determine the protein structures,⁵⁷ and SERS of gold particles can be performed within a single living cell.⁵⁸ SERS is a fresh alternative to quantum dot excitation. Quantum-dots are useful due to their size-dependent fluorescence properties, but the potential toxicity of the semiconductor materials is a major problem.

There are also several research efforts aimed at pushing resolution into the low end nanometer range. Obtaining higher resolution in the far-field is limited by diffraction and the uncertainty principle, which allows the resolution to be approximately $\lambda/2$. Immersing the lens in a higher index of refraction material can further enhance resolution, but most of the sub-wavelength information is obtained through near-field optics. Near-field microscopes are not as easy to use, and images are obtained through point-by-point scanning.⁵⁹ The concept of a perfect lens based on materials with a negative refractive index (negative permittivity and permeability) may offer sub-wavelength resolution by preventing losses of evanescent energy. In plasmonics, recent experiments have also revealed the potential of directional steering of a beam of light using periodic corrugations, such as the bulls-eye image in Figure 15. Appropriately shaped dielectrics on the surface can also potentially act as a magnifying mirror that can enhance the surface resolution.⁶⁰

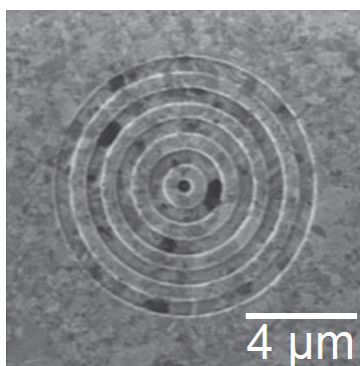


Figure 15: Bulls-eye pattern with a single hole surrounded by periodic corrugations. This structure can exhibit beam steering effects and reduce the diffraction angle to within 3° from center. Analysis taken from [61].

Far-field imaging of DNA, protein molecules, and viruses could be invaluable to the medical imaging community. Tracking these molecules through different cell cycles can provide greater understanding of their roles in normal cell function and disease progression.

2.4. Applications in Cancer Research

Incorporating nanotechnology into cancer biology has involved two major fields: nanovectors for administering therapeutics and imaging systems, and the precise patterning of surfaces. Patterning technology offers the potential for advancements in early detection and diagnosis of disease based on its ability to detect specific molecular signals and biomarkers.⁶² Some of the developed patterning features include nanowires,⁶³ nanocantilevers, and nanotubes. Gold nanoshells can also be used to ablate tumor cells.⁶⁴ Nanoholes are another pattern feature that offers promise in sub-wavelength biosensing. Tumor cells have many mutations in genes encoding for cytoplasmic signaling molecules that modify cell growth and adhesion. Rho GTPases have a major role in locomotion through their modulation of the actin cytoskeleton.⁶⁵ Understanding the participation of these proteins in tumorigenesis can be aided by plasmon enhanced cell surface studies. Tumor markers have been detected based on spectral shifts in transmission peaks using random arrays of nanoholes.⁶⁶

Chapter 3

Materials and Experimental Methods

We began our research with the hypothesis that Nanosphere Lithography could be used as a high-throughput alternative to the fabrication techniques of Focused Ion Beam Lithography and Electron Beam Lithography. The literature has shown electron-beam lithography to be the most versatile method of fabricating these nanostructures, but the cost per sample has still limited widespread application.⁶⁷ In this work, several experiments were performed to manipulate the self-assembly process and improve patterning results for NSL. The sections within this chapter describe our initial experiments in variations of the drop-coat method and spin-coat method, the self-assembly phenomenon, and the method of directed self-assembly. Directed self-assembly is a way of manipulating the entire drop of solution and allow the spheres to self-assembly in desired locations. The over-all fabrication techniques of Focused Ion Beam milling and Nanosphere Lithography are also detailed. Focused Ion Beam was used as a comparative tool for Nanosphere Lithography to generate similar structures.

3.1. Materials

Polystyrene Spheres

We mostly used 1 μm polystyrene spheres to study and improve the patterning method of self assembly. Spheres were ordered from several different companies in a variety of sizes and concentrations, as illustrated by Table 2. The concentration of the spheres in solution ranged from 0.1% up to 4% weight by volume. Ted Pella provides low concentrations of spheres for a cheap price (\$15.00/10mL), which allowed us to test the viability of a variety of different sphere sizes. When using a high concentration of spheres, faster patterning can be achieved; however, we found it very difficult to produce monolayer crystals with a 4% solution. When using a 2.5% concentration, monolayers could be produced consistently, but defects covered a greater percentage of the patterned surface.

Table 2: Polystyrene spheres were purchased from several different companies. The spheres were used without any further dilution.

Company	Sphere Size	Quantity	Weight by Volume	Website
Corpuscular	600 nm	10 mL	2.5%	http://www.microspheres-nanospheres.com
	800 nm	10 mL	2.5%	
Polysciences	600 nm	15 mL	1%	http://www.polysciences.com
	790 nm	15 mL	1%	
Invitrogen (Interfacial Dynamics)	500 nm	15 mL	4%	http://www.idclatex.com
	1 μm	15 mL	4%	
Duke Scientific	1 μm Green	15 mL	1%	http://www.dukescientific.com
	1 μm Blue	15 mL	1%	
Ted Pella, Inc.	260 nm	10 mL	0.1%	http://www.tedpella.com
	300 nm	10 mL	0.1%	
	490 nm	10 mL	0.1%	
	1.08 μm	10 mL	0.1%	

Drop size and the percent weight of solids should be optimized for each experiment. A 1% weight by solids produces the best monolayer in Directed Self-Assembly, but a higher concentration can produce better results in Spin-Coating. The particle count in each drop depends on the size of the spheres and the percent weight. For a fixed concentrations of 1%, the total monolayer packing area increases as the diameter is reduced to a smaller sphere size. The following equation (Polysciences, Inc.) can be used to calculate the number of particles per mL:

$$\begin{aligned}
 \text{Particles / mL} &= \frac{6w \times 10^{12}}{\rho \times \pi \times \phi^3} & w &= \text{grams of polymer/mL (0.01 for 1\%)} \\
 & & \phi &= \text{diameter of latex particles (\mu\text{m})} \\
 & & \rho &= \text{density of polymer (1.05 g/mL)}
 \end{aligned} \tag{34}$$

This equation can be used to calculate the overall patterning area achievable if every sphere were placed down in a monolayer form. The calculations were performed for a drop size of 0.7 μL , which we used consistently in our procedure. We can achieve millimeter sized patterns of monolayers for various sphere sizes.

Table 3: Particle count and patterning area achievable for a fixed concentration of 1% weight by volume.

Pattern Area of Polystyrene Spheres (1% wt. solids)			
Sphere Diameter (nm)	Particles/mL (1% solids)	Particles/Drop (0.7 μL)	Patterning Area (mm^2)
200	7.14E+12	5.00E+09	14.14
350	1.33E+12	9.33E+08	10.69
500	4.57E+11	3.20E+08	8.94
750	1.35E+11	9.48E+07	7.30
1000	5.71E+10	4.00E+07	6.32

Substrates

We first experimented on clean glass slides, which should be soaked in a piranha solution for at least 20 minutes. Piranha solution (H_2SO_4 and H_2O_2 , 3:1) removes any organic material from the surface and creates a very hydrophilic substrate. A hydrophilic substrate is advantageous in our experiments by providing a very small contact angle. This allows the spheres to nucleate at the edge of the meniscus quickly. In some of the early experiments, a hydrophilic substance was also useful in the drop-coat and spin-coating methods because it permitted the solution to uniformly cover the glass surface and allow for a more even deposition of the spheres. In our later experiments, the spheres were patterned on either a photoresist protective layer or directly on the gold surface. Exposing the gold surface to a UV lamp for at least 20 minutes improves the patterning quality, while this has no effect on the photoresist substrate.

3.2. Self-Assembly Experiments

Self-Assembly Phenomenon

Self-assembly is a process in which the forces of evaporation and electrostatic repulsion between colloidal spheres guide the arrangement of spheres into the lowest energy state available. In this natural process, colloidal spheres self-assemble at the meniscus of an evaporating solution due to capillary forces. Lateral capillary forces are due to the overlap of menisci formed around separate particles attached to an interface. Capillary forces, Brownian motion, and electrostatic repulsion all contribute to the final organization of the spheres into arrays, as shown in Figure 16. Attractive lateral capillary forces cause 2D aggregation and ordering in a wide scale of particle sizes: from 1 μm down to 1 nm.

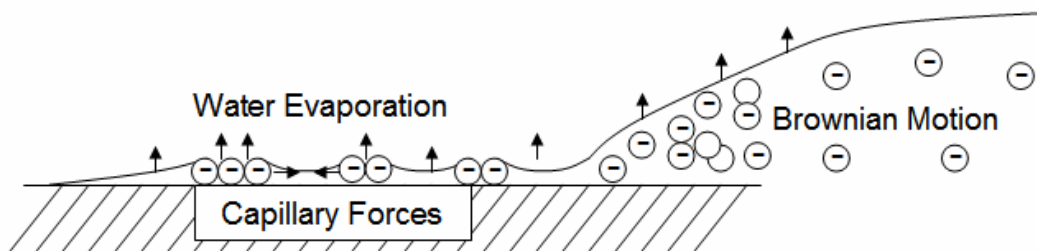


Figure 16: Forces driving self-assembly of nanospheres. Water evaporation creates lateral capillary forces that draw the spheres together.

The first requirement of self-assembly is the nucleation of a crystal. From this point, crystal growth takes place through immersion lateral capillary forces. The capillary forces present relate to the position and shape of the contact line and the wetting properties of the substrate. During evaporation, local sphere density changes in the solution, fluctuations in humidity and temperature, and the lack of a guiding apparatus become major problems that render many areas of the substrate useless. Crystalline defects are a regular occurrence in this type of self-assembly. The distance between defects in polystyrene crystals is typically on the order of 10-20 sphere diameters.

Self-assembly occurs at a receding meniscus of an aqueous colloidal suspension. An optimal balance of physical and chemical forces must be maintained to produce a two-dimensional, defect-free crystalline structure. This usually requires a hydrophilic, smooth substrate, which can limit the possible applications of the technique. Theoretical and experimental studies of nucleation and growth of polystyrene crystals were performed in the early and mid 1990's that allowed several patterning methods to be developed.⁶⁸ Several researchers have attempted to reduce defects by creating temperature and humidity controlled environments, angling the drop,⁶⁹ spin-coating, by creating Langmuir-Blodgett films,⁷⁰ or by controlling the recession of the meniscus line.⁷¹ Two-dimensional crystals can also be aligned in solution by AC fields.⁷²

Two of our initial experiments in using colloidal lithography were in the Drop-coat method and the Spin-Coat method. A fundamental understanding of the nature of Self-Assembly was gained through these studies, but the experimental results were not reliable in producing consistent substrates. Directed Self-Assembly can maintain precise control of the deposition and quality of the assembled monolayer crystals. We modified this technique to produce consistent substrates with apertures in a grid-like microstructure. The experimental methods for these techniques are described in the following sections.

3.2.1. Drop Coat Method

The simplest method of producing a self-assembled monolayer of spheres is to use the drop-coat method. By placing a small drop (1-20 μ L) on a substrate, ambient conditions will cause the solution to evaporate from all sides. When the substrate is hydrophilic, the drop will have a small contact angle. Evaporation at the edges of the drop creates lateral capillary forces, which causes the dispersed colloids to flow towards the sides. When the diameter of the spheres is comparable to the meniscus height, Van der Waals forces pull the spheres to the substrate and they pack in aggregate or polycrystalline form. Although the patterning is random by nature, certain parameters can be controlled to reduced multilayer stacking and line defects. Angling the substrate is one way of improving packing order. This stretches the drop due to the weight of gravity and causes a receding meniscus to form at the top of the substrate. By using a Peltier cooler to reduce the temperature, the evaporation rate can be lowered to allow the spheres time to assemble. The images in Figure 17 show sphere alignment similar to that reported by Dushkin, et al.⁷³ Using an angled substrate improves the patterning towards the top of the substrate, but the density of spheres at the lower edge is increased and aggregates form over the majority of the area. Still another variation of the drop-coat method is to place suspended metallic grids over the drop. This creates capillary forces that draw the spheres to the grid as the fluid level lowers. The image results from this experiment are shown in Figure 19.

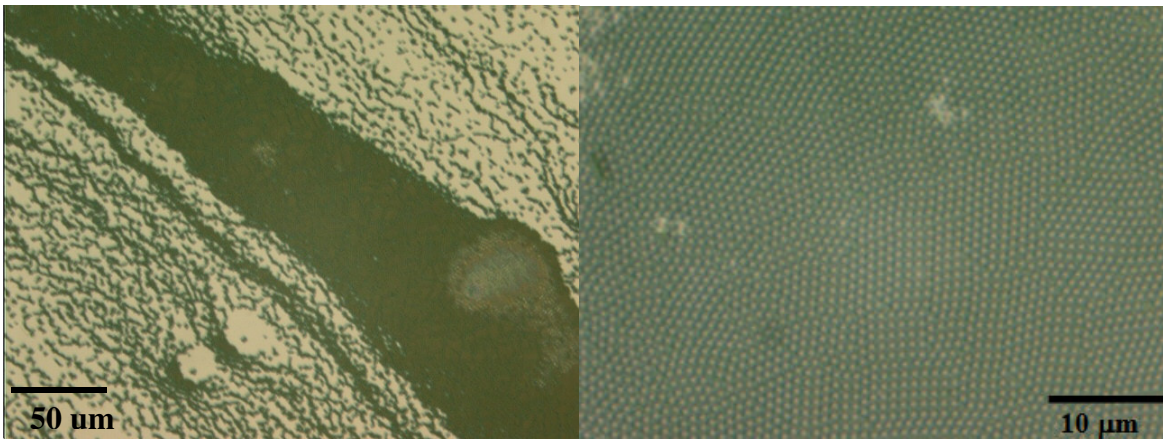


Figure 17: A) Image of the angled drop coat method (5°), which shows many empty spaces and multilayer stacking of the particles. B) Best achievable packing order showing random crystal orientation and some multilayer regions.

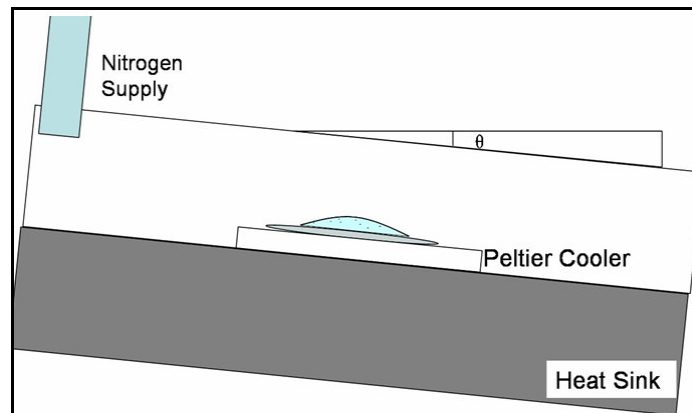


Figure 18: Angled drop-coat method with the use of a Peltier Cooler to reduce the temperature to 2-4°C. Nitrogen supply reduces humidity level.

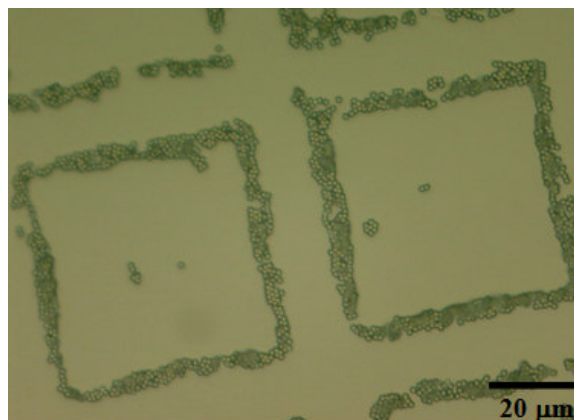


Figure 19: A variation of the drop-coat method is to use copper TEM grids placed over the drop to pattern the spheres.

3.2.2. Spin-Coat Method

Substrates were either cleaned with acetone and methanol or soaked in a piranha solution before spinning to produce a small contact angle and allow the drop to spread evenly. When acetone and methanol was used in cleaning, a slow spin speed produces a wavelike packing order in many of the regions (Figure 21). With a higher density of spheres, these regions should pack into a monolayer crystal. Piranha etching the substrate creates a more hydrophilic substrate, and this wavelike packing is not observed. The Figures from Table 4 are discussed in Chapter 4.

In the spin coat process, it was noticed that around sphere clusters, the packing order improved greatly. With this in mind, we began to explore using pillars of photoresist (AZ 5214E) to obtain regions of highly ordered spheres. Photopillars may help ordering the spheres by providing a higher meniscus that enables a longer nucleation time (Figure 21). Using photoresist on the substrate is also addressed in section 3.2.4. While spin-coating is a fast, simple method of generating monolayers, the location of the patterns produced is still random. Most of the substrate is useless because of widespread defects.

Table 4: Several rpm's were tested for a variety of sphere sizes. Figures are discussed in Chapter 4.

Particle Size (nm)	Revolutions Per Minute	Spin Duration (minutes)	Results
500	600	3	Figure 30
	460	4	Figure 31
	400	4	Figure 32
780	2000	2	Figure 33
	1000	2	Figure 34
	500	3	NA
	250	4	Figure 35
1000	600	4	Figure 36
	500	4	Figure 37
	400	4	Figure 38
	300	4	Figure 44

* All substrates were soaked in a Piranha etch solution for 1/2 hour before use.

Drop sizes were 1 μ L and 1% solids by volume

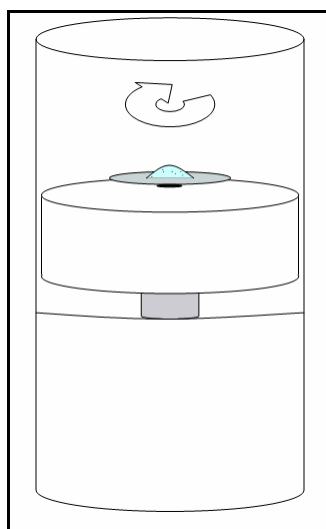


Figure 20: Spin coating polystyrene spheres was performed with varying speeds (250rpm-4000rpm). A speed of 460 rpm's proved to be most consistent with various sphere sizes. The substrate is spun until dry.

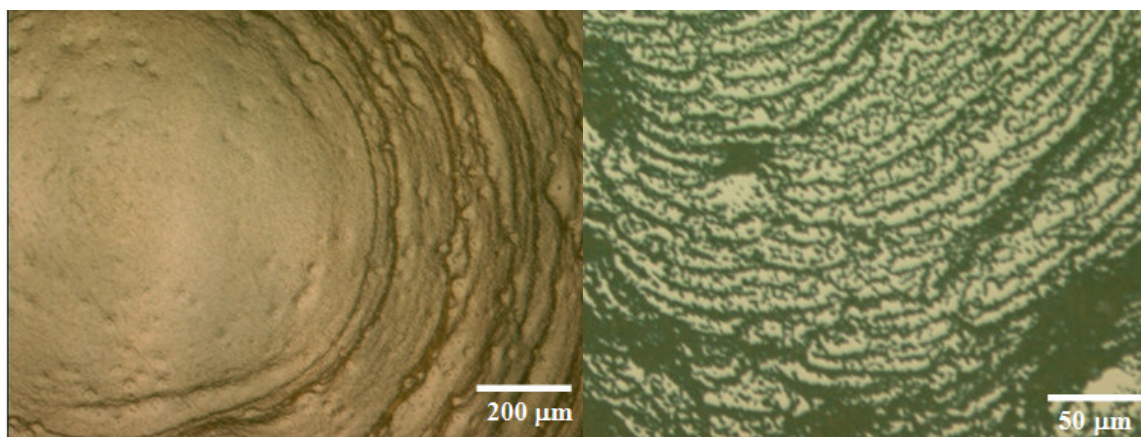


Figure 21: Left) Spin-coating results in multilayer stacks at the periphery and wavelike packing throughout the coated areas. Right) Drying at low rpm's (< 500) results in a wavelike effect in the less dense regions.

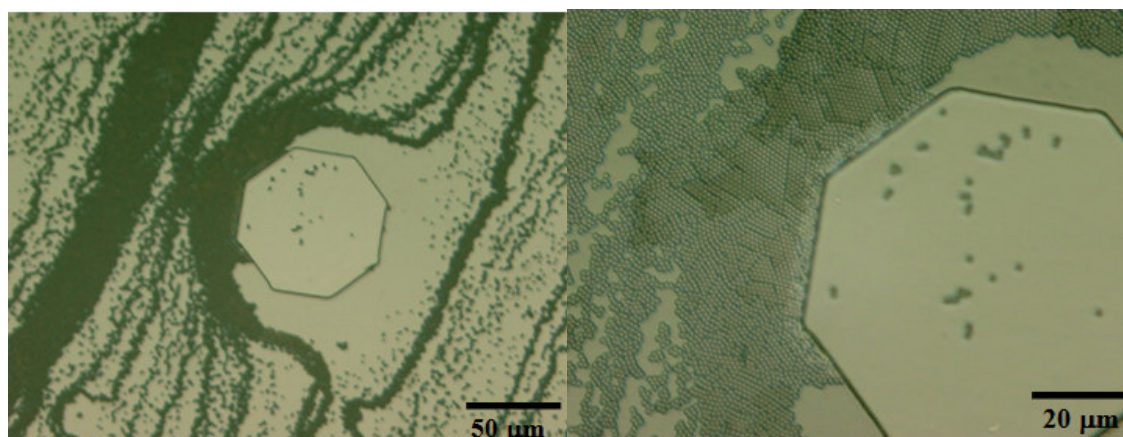


Figure 22: Left) Spin-coating around hexagonal shaped photopillars Right) Zoomed image shows polycrystalline order around along the edges and extending out from the photopillar.

3.2.3. Directed Self-Assembly

We adapted a liquid drop dispenser, the Bioforce Nanoarrayer, to control the self-assembly of polystyrene spheres. The Nanoarrayer was originally designed to place small drops of protein-solution on a substrate. The machine proved to be difficult for use in dispensing small drops of colloidal solution due to the rapid drying and clogging of the cantilever tip. We instead used the stepper-motor and real-time video capabilities of the system to manipulate the meniscus line of a 0.7 μL drop of colloidal solution. The Nanoarrayer can also maintain precise control of the relative humidity.

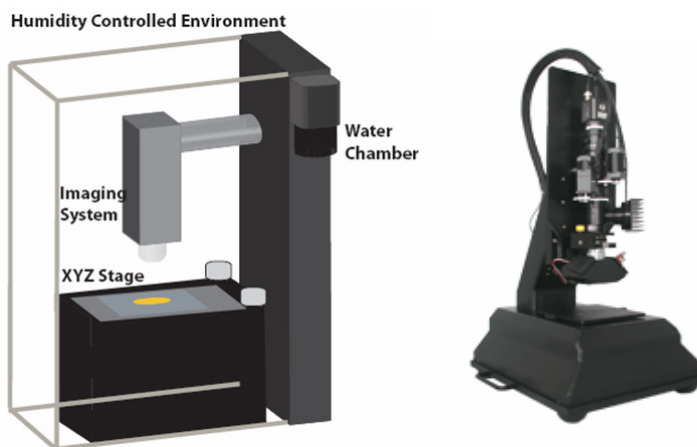


Figure 23: Diagram and image of the Nanoarrayer tool used for directing self-assembly of polystyrene spheres.

In the method of directed self-assembly, no real advantage was gained through piranha etching the glass. This is because once nucleation takes place, the spheres will continue to self assemble into crystalline form at the rate of the stepper motor. Later experiments also showed that patterning spheres on the surface of a thin layer of photoresist is also possible. The surface chemistry of gold was also explored for improvements in packing of the spheres. Once nucleation occurs, spheres can pack very well on a gold surface. From these studies, it seems that a hydrophilic surface is very important in establishing control of the nucleation site. However, once the spheres begin to pack, due to constant evaporation, the spheres will assemble into a crystalline structure regardless of the hydrophilic/hydrophobic nature of the substrate.

Our method of directing self-assembly first began by exposing a silicon nitride edge to a UV lamp for 20 minutes creates a hydrophilic surface to hold a drop of colloidal solution (0.7 μL). After placing a drop on the surface, the edge is then lowered to the substrate by a

computer control to the surface and dragged along in a step-wise fashion. The rate of stepping is adjusted by visually confirming the assembly of good, periodic structures. This technique relies on the self-assembly of polystyrene spheres, which are then used as a shadow mask in the deposition of a gold layer.

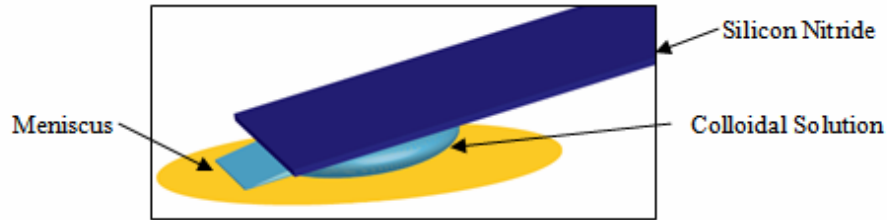


Figure 24: Silicon Nitride surface with a colloidal solution being dragged to the surface of a substrate. The meniscus has become a straight line parallel to the Silicon Nitride edge.

The hydrophilic edge creates a horizontal meniscus line, rather than circular. This reduces the density imbalance of spheres along the assembly line as the meniscus recedes. By controlling the recession and advancement of the meniscus, the crystal growth can be regulated. A similar type of process has also been explored by other groups,⁷⁴ although a constant velocity was applied and visual control of the system was not maintained, as in our system.

In our experimental set-up, we have worked with a particle volume fraction of $\phi = 0.01$. The volume fraction of the particles in the area that we want is represented by ϕ_a . Our crystal thickness is $h = 1 \mu\text{m} = 2R$, for a monolayer. The β term accounts for the fact that the convection velocity of the particles may be different from the hydrodynamic velocity of water. The b term is the width of the wet array, which in our case was approximately $20 \mu\text{m}$. The ratio of $b/2R$ determines the height of the hydrophilic plate that should be maintained. In the majority of our experiments, this ratio equaled approximately $10 \mu\text{m}$. The velocity of the contact line is step-wise rather than continuous, but for a 1% solution of spheres, the velocity was experimentally determined to be $2 \mu\text{m}/\text{sec}$.

$$v_c = \frac{\beta \times j_c \times V_w \times \phi \times b}{2R_p \phi_a (1 - \phi)} \quad (\text{for monolayer}) \quad (35)$$

Forcing the spheres to nucleate on the substrate before dragging eliminates the need for a hydrophilic substrate, and chemical templates can also be incorporated to improve patterning. Sandwiching the drop between two hydrophilic plates can allow for a continuous feed of spheres,⁷⁵ but this technique was not explored.

3.3. Modified Nanosphere Lithography

3.3.1. Processing Techniques

Through Directed Self-Assembly, millimeter areas of spheres can be organized into a continuous monolayer using only a small drop of solution. But self-assembly still produces regions with many flaws, as shown in Figure 25. Efforts were undertaken to reduce these defects using a pre-patterned surface. A small step height establishes potential energy wells for the spheres to organize within. Using a photolithographic mask with feature sizes smaller than 20 times the sphere diameter to pre-pattern the substrate, defects can be significantly reduced. The photolithographic features create periodic grain boundaries, and reduce the number of propagating defects. In these experiments, 1 μm spheres were predominately used and the typical defect free regions extend to 20 μm . But this technique can be extended to any sphere size by adjusting the step height to less than half of the sphere diameter. The pre-pattern features must be adjusted for the sphere diameters to be used. When the feature sizes are integer multiples of the sphere size, the packing contains far fewer defects. A variety of shapes were defined through photolithography to include squares, triangles, rhombi, and circles, as illustrated in Figure 26.

Self-assembly occurs over both the gold regions and in the glass wells. A pre-patterned substrate can reduce crystalline defects, but protecting the surface layer from forming rough surface features is also important. These rough surfaces could cause optical effects due to localized plasmon coupling. To confine the patterned regions to only the glass wells, we protected the gold surface with a layer of photoresist before depositing the spheres, as shown in Figure 27. We used a thinned photoresist layer (AZ 5214E + PGMEA) to protect the pre-patterned gold surface from the spheres, as shown in Figure 27.

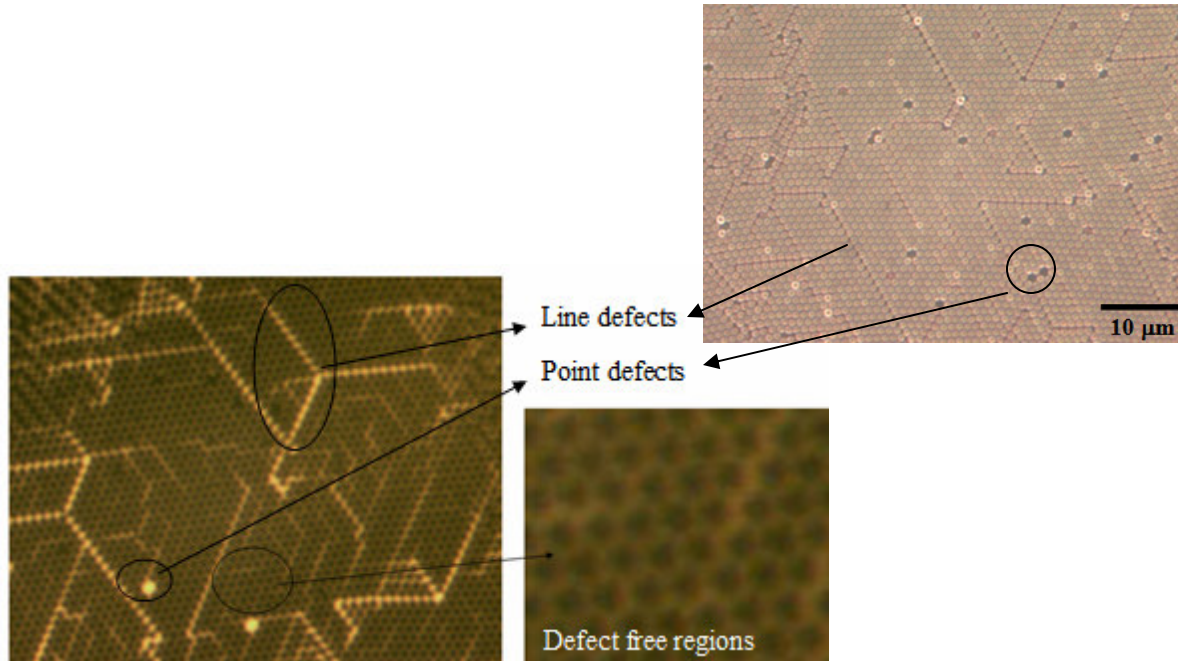


Figure 25: Many defects are noticeable due to packing flaws in self-assembly.

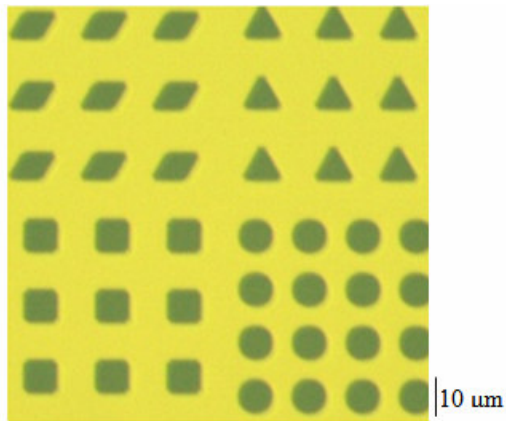


Figure 26: Pre-patterned substrate using a variety of features as deposition wells for the spheres.

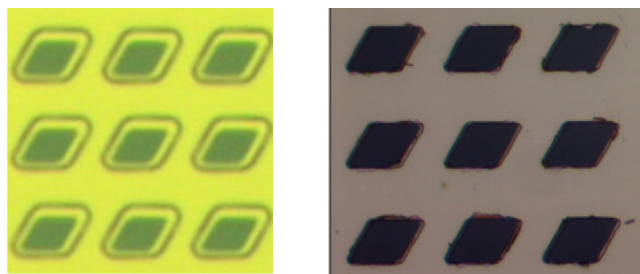


Figure 27: A thin layer of photoresist protects the gold substrate. A) Notice the mismatch between the size of the glass and the photoresist features. B) Optimizing the exposure times eliminated this defect.

Using a pre-patterned substrate requires two metallic film depositions. The first deposition creates an optically thick pre-patterned substrate, while the second is used for the features within the geometric patterns. After a second metallic deposition, the spheres and photoresist can be lifted off to reveal nanometer features within a micropatterned grid. The flow diagram in Figure 28 shows the overall modified process of NSL to create reduced defect patterns in specific locations of a substrate.

The flow diagram in Figure 28 is an adjusted method for Nanosphere Lithography that can be used to obtain periodic apertures aligned in a micron scale grid. The mask used in photolithography can have any kind of surface features, though an integer multiple of the sphere size being used will likely improve patterning results. The sphere deposition step takes advantage of directed self-assembly method, as previously described. Before depositing the spheres, special care was also taken to align the pre-patterned features at right angles to the direction of the receding meniscus. Since the meniscus along the edge forms a straight line, the crystalline packing can be obtained uniformly over a wide lateral distance (2-3 mm).

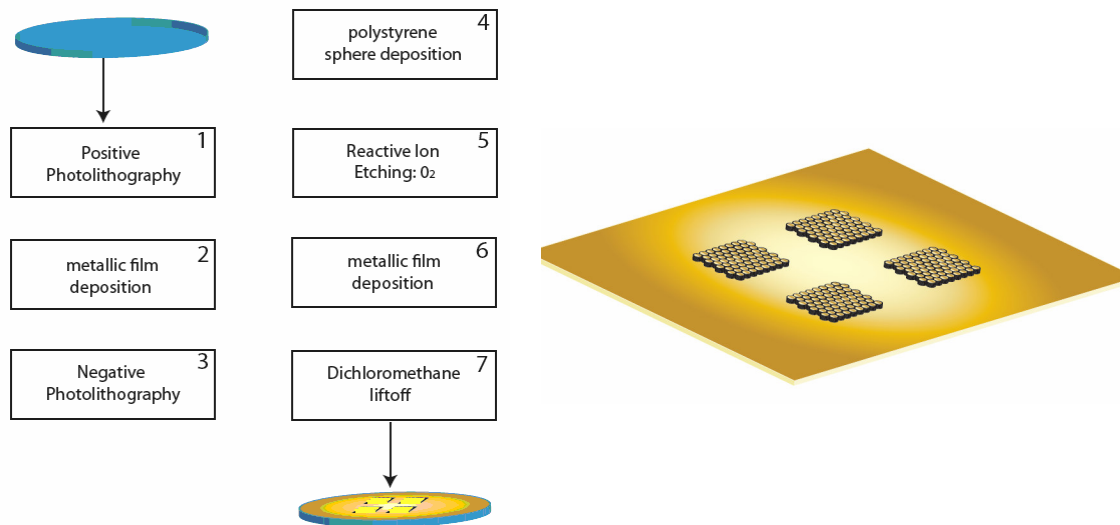


Figure 28: Flow diagram of fabrication process using five basic techniques: photolithography, metal deposition, sphere deposition, etching, and chemical liftoff. This produces hexagonal periodic holes in regions specified via photolithography.

3.3.2. Reactive Ion Etching

After depositing the spheres onto the substrate (Figure 25, step 4), the sphere surface can be etched to create spaces between the spheres (step 5). A second metallic deposition will then create hexagonal spaced apertures instead of nanoparticles. Reactive Ion Etching of polystyrene spheres is accomplished through the use of oxygen plasma. The spheres were exposed for a range of times between 0.5 seconds and 2.5 minutes. Charging of the spheres can become a problem for longer exposure times. For example, Figure 58 shows a dark field image of the clumping of spheres due to an exposure time of 2.5 minutes for 1 μm spheres. By performing the etching process in steps this effect can be reduced. By Reactive Ion Etching the polystyrene spheres, the radii of the spheres can be reduced to allow connection of metallic islands by thin veins. This establishes nanometer sized apertures with a much smoother topology.

Table 5: Reactive Ion Etching of polystyrene spheres with O₂ plasma. Several different exposure times were tested for different sphere sizes for a fixed gas pressure.

Reactive Ion Etching Polystyrene Spheres			
Sphere Diameter (nm)	Total Etch Time (min)	Etched Sphere Diameter (nm)	Results
1000	1:30	950 nm	Figure 47
1000	2:00	850 nm	Figure 49
1000	2:30	800 nm	Figure 51
1000	3:00	650 nm	Figure 53
780	1:30	600 nm	Figure 55
780	2:00	400 nm	Figure 57
780	2:30	Aggregation	N/A
780	2:45	Aggregation	N/A
500	0:30	Aggregation	N/A
500	1:00	Aggregation	N/A
500	1:30	Aggregation	N/A

3.4. Focused Ion Beam Lithography

Focused Ion Beam milling was performed by a Hitachi FEI Quanta 200 3D, with dual column SEM imaging capabilities. The FIB uses liquid Gallium as an ion source because of its low melting point (room temperature) and high focusing capabilities (< 10 nm). The ion beam can also be used as an imaging tool by collecting the secondary electrons scattered from the surface; however, sputtering of the sample occurs. SEM imaging prevents the destruction of the surface, which is crucial for the studies performed here.

Our group explored the Focused Ion Beam method because it can be optimized to produce perfect periodic structures from an image template. The image software reads a 512×512 , 24-bit monochrome bitmap file that we designed to produce periodic particles and holes (Figure 29). Sputtering conditions were optimized for different thicknesses of the gold film, which ranged from 100 nm to 250 nm. A low beam current of 10 pA was typically used with exposure times of up to 5 minutes, depending upon the size scale of the features. The deposition parameters, such as beam current and exposure time, need to be optimized for each structure. Figure 13 shows a set of ellipses of varying diameter. The larger holes (bottom right) have been milled completely, while the smaller set (left three columns) has not been fully penetrated. Further exposure would cause the lines between the holes to deteriorate and form lines.

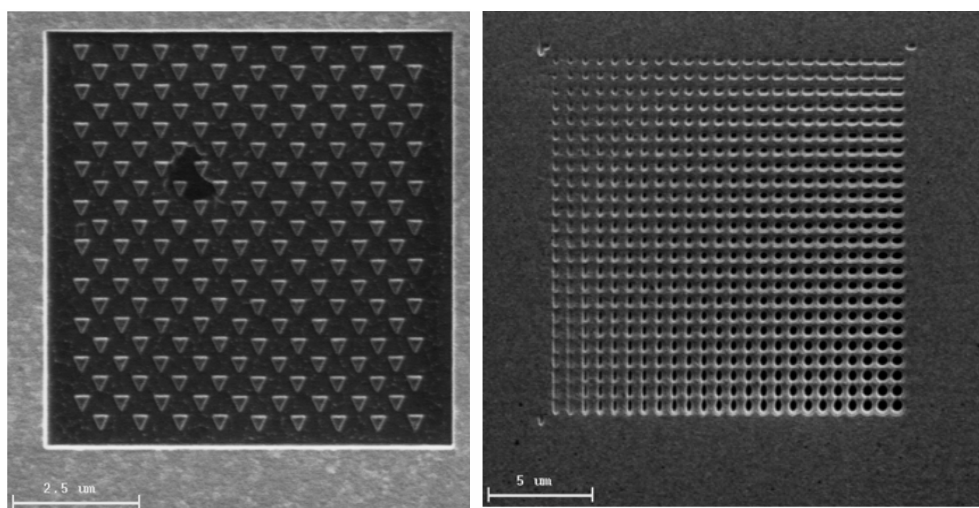


Figure 29: (A) periodic particles fabricated by Focused Ion Beam milling in 180 nm thick gold film. (B) SEM image of an array of holes with different dimensions, generated through Focused Ion Beam Milling.

3.5. Fabrication & Analytical Equipment

All of the metallic films for our experiments were deposited with an Edwards Auto 306 E-beam. The deposition takes place under vacuum pressures of approximately 3×10^{-5} Torr, and the substrate is rotated above the crucible to generate an even thickness. The film thickness is controlled by a quartz crystal monitor and calibrated for the density of gold. Photolithography steps were performed using an MJB 3 Karl Suss photoaligner. The exposure times and baking conditions are optimized for AZ 5214E Image Reversal Photoresist. The resist can be thinned to the desired spin height by mixing different ratios of Propylene Glycol Monobenyl Ether Acetate (PGMEA) with the resist. Positive photolithography required an exposure time on glass of 8 seconds for the un-thinned layer. In negative lithography on a gold surface, 2 seconds exposure time and 50 seconds development were the optimized conditions. A Plasmalab 80 Plus Reactive Ion Etching machine was used for surface modification of the polystyrene spheres. The spheres were exposed to a process pressure of 30 mTorr with 50 sccm O₂. RF forward power was maintained at 100 Watts, and the process time was adjusted between 0:30 and 3:00 minutes.

The analytical tools used were a Dimension 3100 Atomic Force Microscope, JSM-6400 Scanning Electron Microscope, and an Olympus BX60 Optical Microscope with dark field imaging capabilities. Scanning Electron Microscope images were also provided by the Analytical Instrumentation Facility. AFM can achieve angstrom resolution in the z axis and has a lateral resolution of approximately 10 nm. Thus, the topology of the structures generated by Focused Ion Beam and Nanosphere Lithography can be characterized well, while SEM provides a more true representation of the lateral dimensions of the sample. To characterize the thickness of the metal films deposited, a Dektak 3030 height sensor was used. In the Dektak, a stylus is scanned along a test sample to determine the step-height of the film with accuracy down to a few nanometers. Optical experiments were performed using an Ocean Optics Spectrometer and a Perkin-Elmer Spectrophotometer.

Chapter 4

Results and Discussion

Several different experiments in self-assembly were tested to determine the best overall method for producing high quality 2-D crystals. Hexagonal packing from self-assembly has been used to form a triangular lattice of apertures. The tunability of the system is achieved by altering sphere size, reactive ion etching parameters, and thickness of the metal film. These structures are compared to similar apertures produced with Focused Ion Beam and evaluated for their potential in biosensing experiments.

4.1. Patterns in Self-Assembly

Experimental results from drop-coating, spin-coating, and directed self-assembly are discussed in the following sections. Adjustments in temperature, humidity, and surface chemistry all have a drastic effect on the quality of the crystals produced. The best and reliable patterning method proved to be directed self-assembly, and this method was used in the modified nanosphere lithography steps described in section 3.3. The results from modified nanosphere lithography are discussed in section 4.2

4.1.1. Drop-coat and Spin-coat

The dynamics of the Self-Assembly process were explored for Nanosphere Lithography. The many different methods tried include: drop-coat, spin-coat, physical templates, chemical templates, and mechanical control of the drop. Angled drop coating with temperature and humidity control created more regions of monolayers, although the angle at which the drop was placed did not seem to have as much of an effect as the temperature control.

Spin-coating a drop of colloidal solution reduces the Brownian motion and produces a radial flow. The revolutions per minute used can be roughly divided into two groups. Below 500 rpm's, the drop does not spread out considerably and there is simply a small radial force applied to the spheres. This improves packing by providing an extra force component to the

capillary forces. When the rpm's exceed 500, the drop is spread in many directions (dependent upon exact speed and balance of spinner), which results in random placement of the spheres all the way to the exterior of the substrate. At the edge of the substrate, spheres can assembly into monolayers and multilayers.

Using metallic templates suspended over the drop is an option that was explored as well.⁷⁶ Gold and Copper TEM grids attract most of the spheres by forming capillary suspension bridges between the substrate and the wires. Several chemical templates can be used in combination with this method, however, there is not fundamental way of controlling the density of spheres that assemble beneath the wire-grids.

It became obvious that the drop coat and spin coat methods were inaccurate for obtaining the kind of precise placement necessary, yet much was learned from these experiments. Humidity control proved to be the most important factor in determining crystalline quality for Directed Self-Assembly.



Figure 30: 500nm spheres spun at 600 rpm's. The edge of the substrate shows levels of highly stacked spheres.



Figure 31: 500nm spheres spun at 460 rpm's. Drop no longer spreads to the edge of the substrate

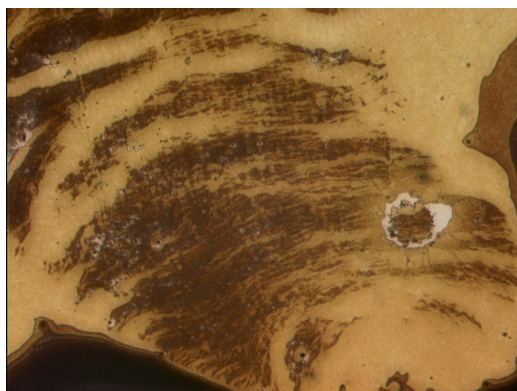


Figure 32: 500nm spheres spun at 400 rpm's. Peach colored areas show monolayers. Darker regions are multilayers.

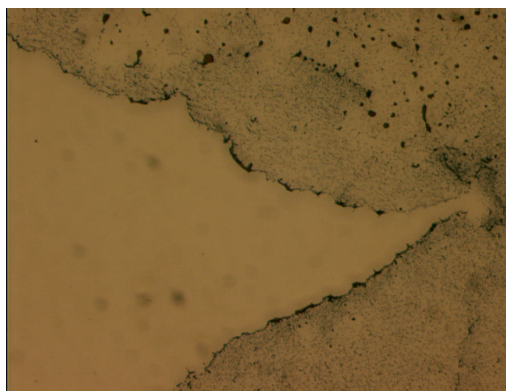


Figure 33: 780nm spheres spun at 2000 rpm's. Center of the drop diverges towards the edge of the substrate.

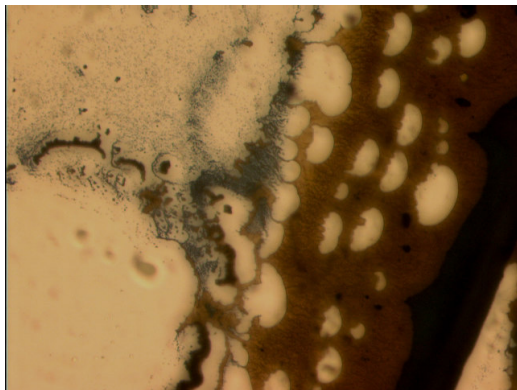


Figure 34: 780 nm spheres spun at 1000 rpm's. Monolayers formed at the edge of the substrate.

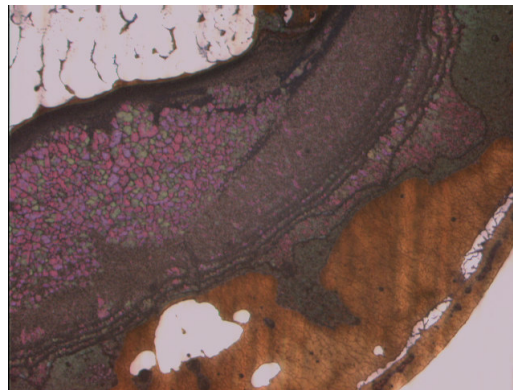


Figure 35: 780 nm spheres spun at 250 rpm's. Edge of the drop is still in the center of substrate, and multilayer stacks dominate.



Figure 36: 1000 nm spheres spun at 600 rpm's. Stacking begins at the edge of the substrate.



Figure 37: 1000 nm spheres spun at 500 rpm's.



Figure 38: 1000 nm spheres spun at 400 rpm's.

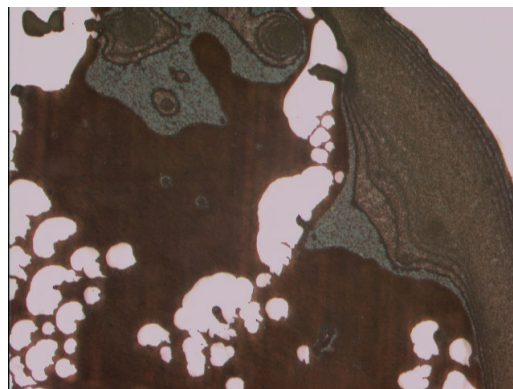


Figure 39: 1000nm spheres spun at 300 rpm's show multilayer stacks at the edge of the droplet.

4.1.2. Directed Self-Assembly

In Directed Self-Assembly, a 1% concentration proved to have the best results by allowing the step rate to be slower, but timely. A 2.5% concentration of spheres also achieves good results with a higher humidity. By dragging the drop quickly, almost no spheres are deposited on the substrate, as shown in Figure 40A. When the drop is wedged between the substrate and a hard edge, the meniscus is a straight line (Figure 41). Depositing the spheres with right angle features could prove useful in optical waveguides.

Stepping the meniscus at a slow rate can produce a single monolayer crystal, as shown in Figure 40B. It is also possible to draw the meniscus back over areas that did not pack tightly. This self-correcting aspect is the real advantage of having visual control over the process. Automation of the process is possible using the color variations at the meniscus line, where self-assembly occurs. Color change along the evaporation line also allows for patterning of sub-wavelength sized spheres. While individual spheres of 300 nm diameter cannot be seen, monolayers and multilayers were formed using this technique.

Directly patterning the substrate before depositing the spheres is another method of controlling the locations of the nanostructures. Mechanical control of the drop allows for complete control of the site of self-assembly, which proved most consistent at reducing defects when applied to a micron-sized pre-patterned substrate. The use of a pre-patterned substrate has been explored in the literature,⁷⁷ but not at the scale of manipulating the crystalline packing structure.

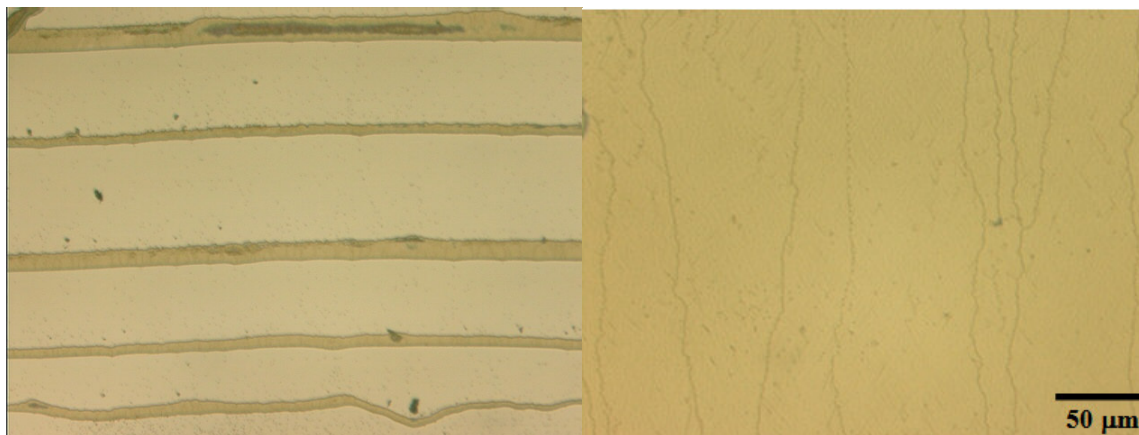


Figure 40: Dragging the meniscus allows a sophisticated level of control as to where self-assembly occurs. A) Lines of various thickness are produced by dragging the drop quickly and pausing at selected areas. B) Continuous monolayers can be established by dragging the drop at slow rates ($1\sim 2\ \mu\text{m/s}$). Vertical lines in B) show propagating line defects.

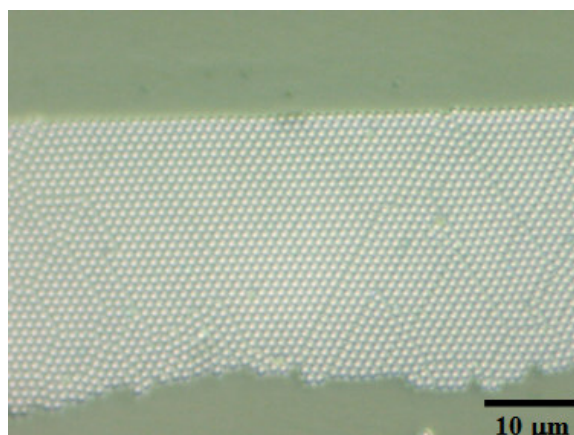


Figure 41: Directed Self-Assembly shows a hard edge can be made with a straight meniscus.

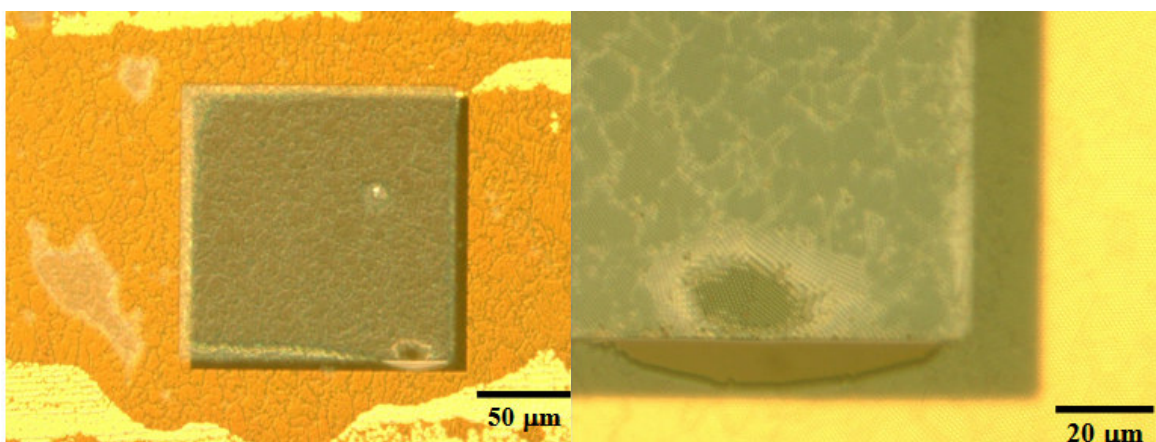


Figure 42: A glass substrate is pre-patterned by photolithography steps to establish square openings in optically thick gold. The depth of the glass wells determine the number of sphere layers that stack together. The step-height was $2\ \mu\text{m}$, and by moving the meniscus slowly a double layer was formed.

4.2. Fabricated Plasmonic Structures

Modified NSL

The Directed Self-Assembly is an effective way of obtaining millimeter sized areas of tightly packed monolayers. This method can be used on many different substrates, provided enough time is allowed for nucleation of the crystal to begin. When the substrate is more hydrophobic in nature, a fast stepping rate can be used to actually channel spheres into desired regions. Using a pre-patterned substrate can further improve crystalline order. Our initial experiments with pre-patterned substrates of 100 μm squares had no effect on the packing arrangement of the spheres. Propagating line defects, slip dislocations, and vacancies were still present. Reducing the mask features to the order of 10-20 times the size of the spheres can actually improve the crystalline structure. At this scale, however, the risk of producing double layers increases due to a high step-height.

Our main objective was to obtain a monolayer packing order, so one difficulty in our process was keeping the step height of the glass wells appreciably small, yet optically thick. If the height exceeds the sphere size, there is a higher probability of developing a multilayer, as in Figure 42. This translates into a minimum sphere size based on the height of the pre-patterned material, and the protective photoresist layer. One way of reducing this limitation is to thin the photoresist. By mixing equal parts AZ5214E photoresist with PGMEA, we were able to reduce the photoresist height from 1.4 μm to 400 nm. With a 100 nm gold deposition, this allows us to use 500 nm spheres.

Fabricating microstructures 10 to 20 times the size of the spheres can present another problem. At this scale there are a limited number of apertures produced in the final product, and optical fringe effects can lead to propagating plasmon modes and thus alter the transmission spectrum. Unpredictable absorption and re-emission can occur.⁷⁸ To reduce the potential occurrence of fringe effects, the pre-patterned substrates can be layered with chrome, which quenches propagating plasmons.

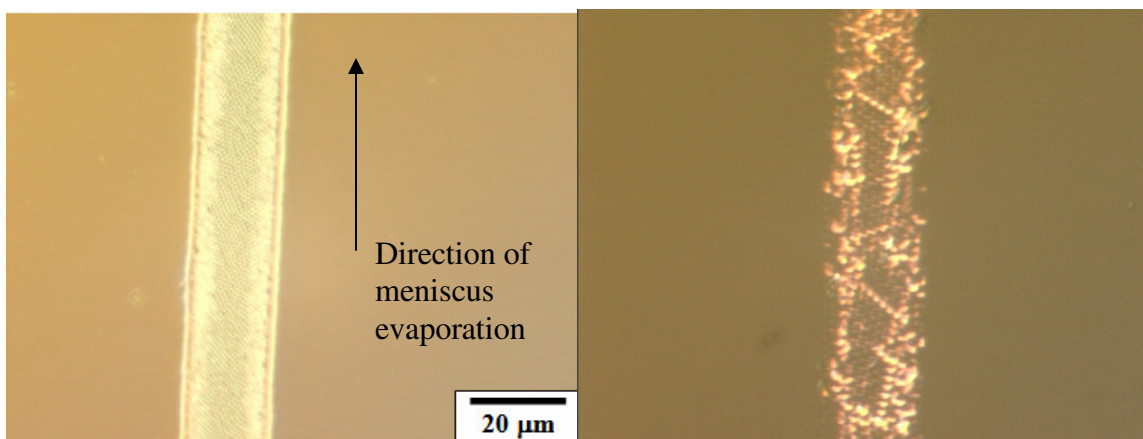


Figure 43: Photolithography was used to create 20 μm channels. By rapidly dragging the drop along the surface, the glass line acts as a funnel for the spheres to assemble in. Control of assembly is limited, but no spheres deposit in the surrounding regions.

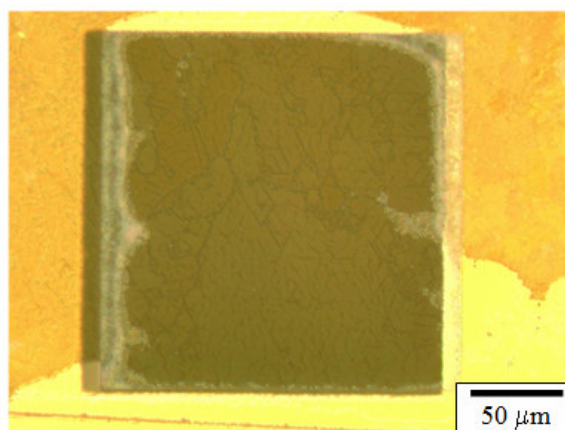


Figure 44: A 100 μm square in a pre-patterned substrate. The location of the spheres can be controlled by mechanically steering the drop and protecting desired regions by photolithography masks.

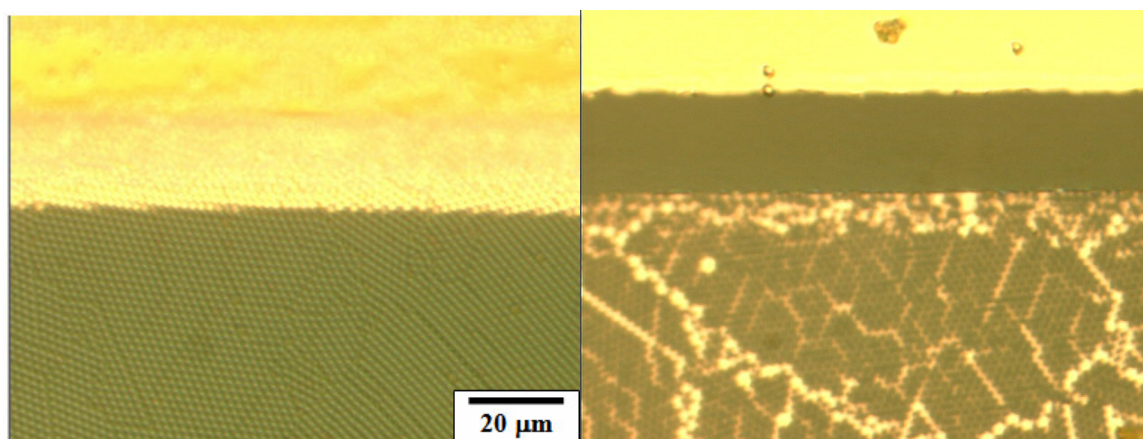


Figure 45: A) The step between photoprotected gold and the exposed glass wells. B) Misalignment in photolithography can result in unpatterned regions.

Reactive Ion Etching

Varying the etching time can tailor the hole sizes. In the literature, reactive ion etching of polystyrene spheres showed an etch rate of approximately 50 nm per minute for 500 nm beads.⁷⁹ When viewed under the Scanning Electron Microscope, it is obvious that the spheres have a shadowing effect even after Reactive Ion Etching. This creates in a sloping profile for the gold structures, unlike the cylindrical tunnels produced through FIB. The hexagonal packed spheres leave several features after liftoff: hillocks remaining from the polystyrene spheres, rings that remain from the organic solutes in aqueous suspension, and triangular posts from the material deposition.⁸⁰ The SEM image reveals these hillocks in the center of the holes. It also reveals a gradient of gold thickness, rather than a uniform step-height. This shape alteration could affect coupling between the front and backside of the thin film. Annealing could be implemented to smooth the film as a final step. While no specific geometry is necessary to generate plasmonic bands, geometric effects will change the location and intensity of transmission peaks. This gradient profile could be the reason why the structures do not scatter light similarly when exposed to the same optical light source.

While the AFM shows definite improvement in the smoothness of the film after Reactive Ion Etching the spheres, care is taken not to draw fast conclusions from this process due to the way the lateral data is gathered. In AFM, sometimes the particles can appear to be closer together because of the convolution of the shape of the nanoparticle with the rounded AFM tip.⁸¹



Figure 46: 1 um spheres

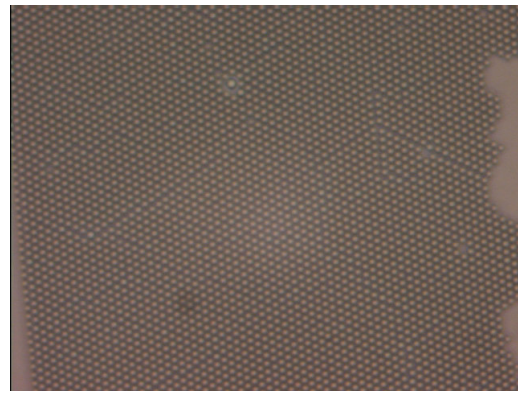


Figure 47: Etch (1:30) reduces spheres to 950nm



Figure 48: : 1 um spheres



Figure 49: Etch (2:00) reduces spheres to 850nm



Figure 50: : 1 um spheres



Figure 51: Etch (2:30) reduces spheres to 800nm



Figure 52: : 1 um spheres

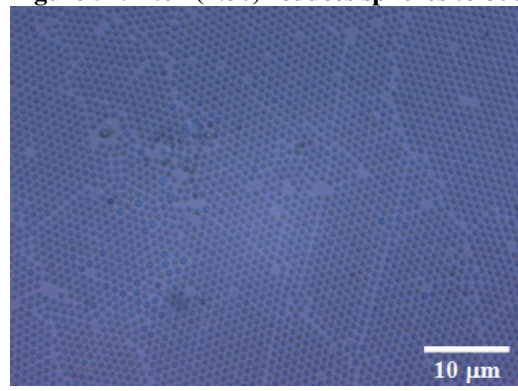


Figure 53: Etch (3:00) reduces spheres to 650nm

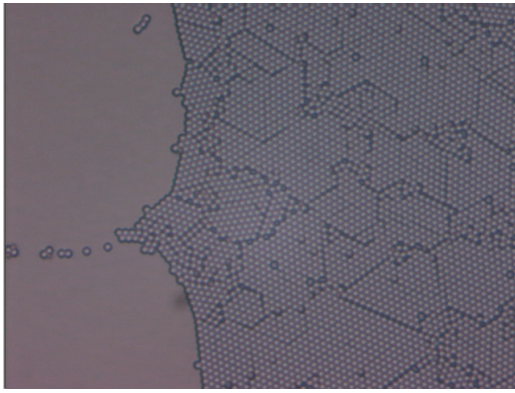


Figure 54: 780 nm spheres

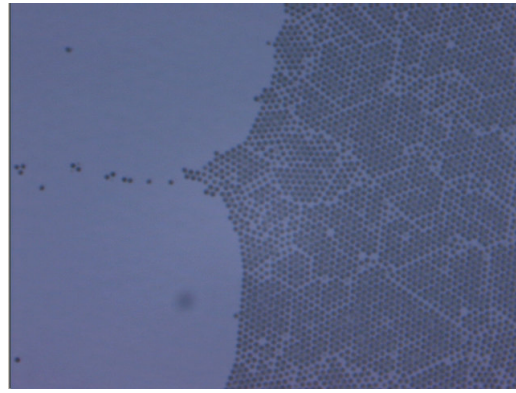


Figure 55: Etch (1:30) reduces spheres to 600nm



Figure 56: 780 nm spheres

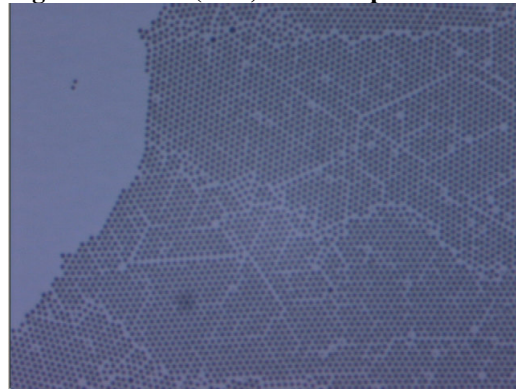


Figure 57: Etch (2:00) reduces spheres to 400nm

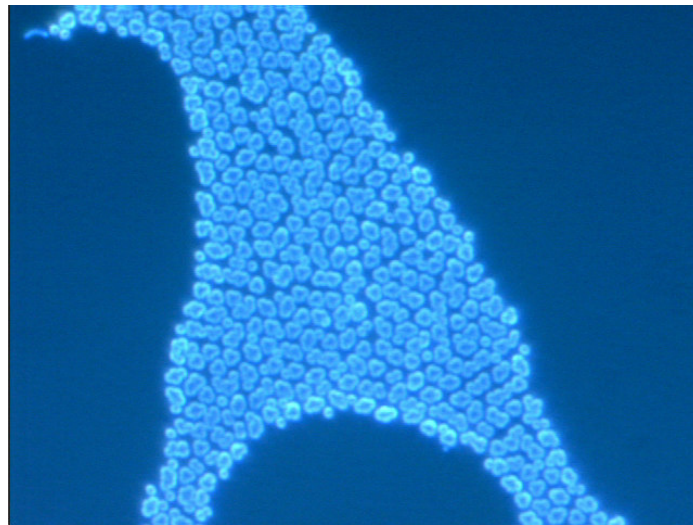


Figure 58: Dark field image of 1 μm polystyrene spheres that shows clumping after 2:30 exposure to O₂ plasma etch.

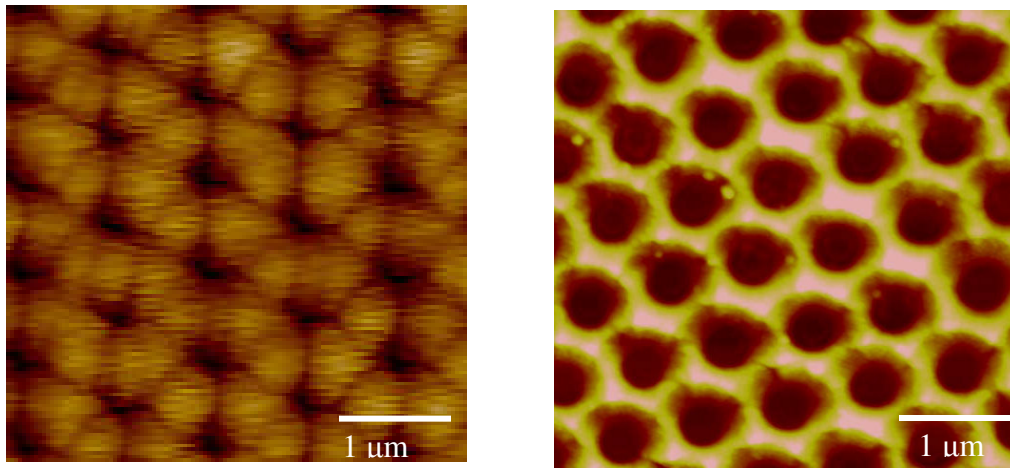


Figure 59: AFM image of holes remaining after liftoff without reactive ion etching (left) and with Reactive Ion Etched spheres. The film shows a higher degree of uniformity when reactive ion etching is used.

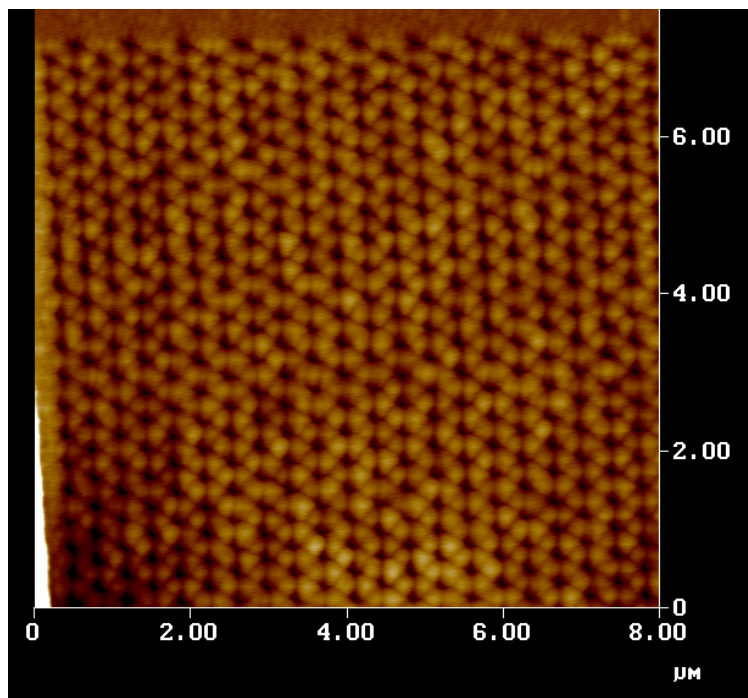


Figure 60: AFM image of holes fabricated by Focused Ion Beam Milling.

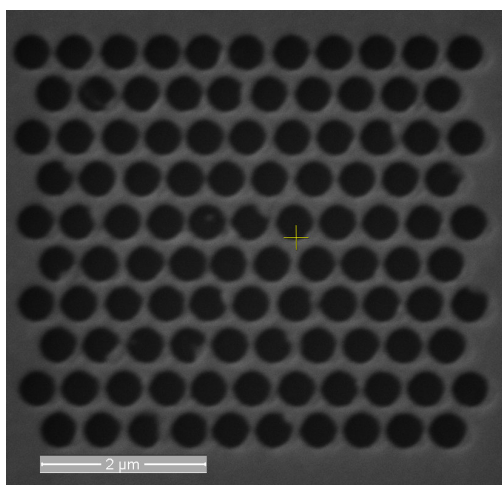


Figure 61: 500 nm holes milled in a hexagonal arrangement similar to NSL using 500 nm spheres.

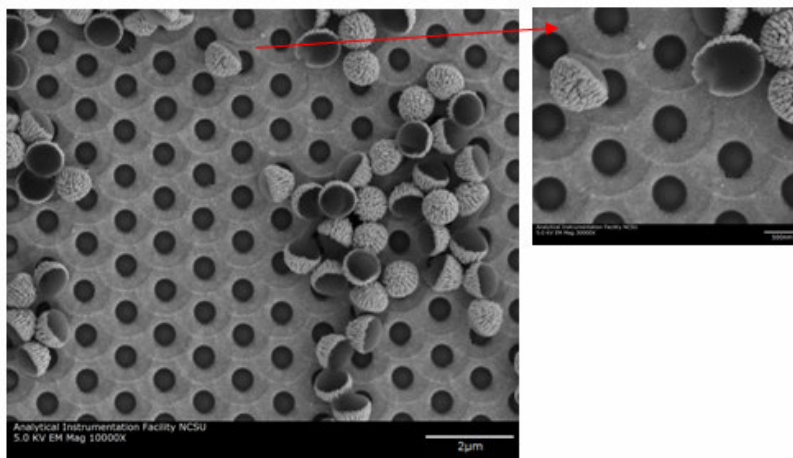


Figure 62: Liftoff via Dichloromethane (CH_2F_2) reveals several hollered out and partially melted polystyrene spheres still held intact by the gold particles. The hole diameters are 500nm using 1 μm spheres.

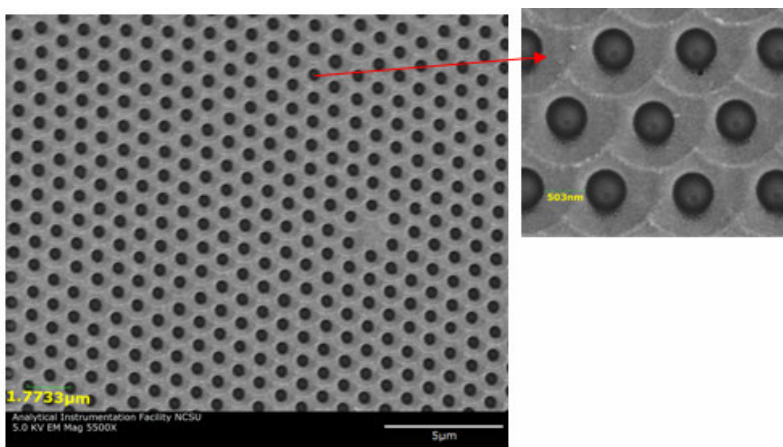


Figure 63: Reactive ion etching the spheres before deposition results in uniform hole sizes in gold film. The centers of the holes also reveal what may be polystyrene hillocks that remain after chemical lift-off.

4.3. Tunable Transmission Spectra

When the metal film is corrugated, the surface plasmons experience band gaps. A periodic structure allows certain standing modes to be established and creates intense electromagnetic fields at the periphery of the apertures. Most of the patterns produced in the literature are ones that offer simple mathematical analysis, such as the square lattice of holes shown in Figure 48A. Lattices fabricated by Nanosphere Lithography have triangular symmetry. Triangular lattices (Figure 48B) can also be treated mathematically in a similar way to square periodic holes.

Triangular lattices have a different rotational symmetry and will show a different transmission spectrum from square periodic structures. Because photon coupling is vectoral by nature, this introduces the possibility of polarization dependence on transmission. The maximum and minimum transmission spectra for periodic structures are a function of the scattering order, as shown in Table 3.⁸² For square and triangular arrays, the peak wavelength transmission at normal incidence depends upon the periodicity of the holes, P , the space between the nearest neighbor a , the dielectric constant of the material, ϵ_d , and the diffractive scattering order (i, j) .

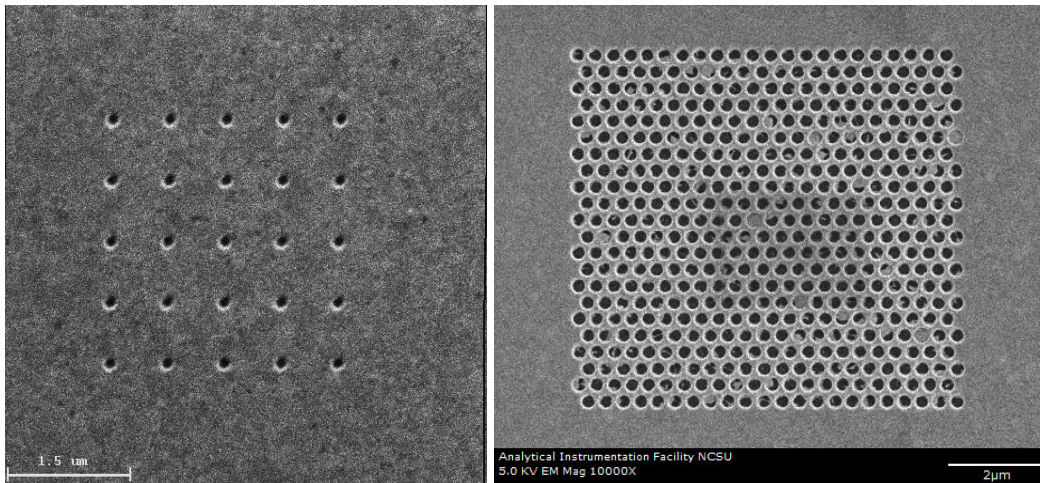


Figure 64: Focus Ion Beam A) square lattice with 200 nm diameter and 500 nm periodicity, B) triangular lattice with 250 nm diameter and 350 nm periodicity.

Table 6: Maximum and minimum wavelengths based on periodicity of square and triangular apertures.

	λ_{\max}	$\lambda_{\min} = \frac{2\pi n_d}{G_{mn}}$
Triangular Lattice	$\frac{P}{\sqrt{\frac{4}{3}(i^2 + ij + j^2)}} \sqrt{\frac{\epsilon_m \epsilon_d}{\epsilon_m + \epsilon_d}}$	$G_{mn} = \frac{4\pi}{\sqrt{3}a} \sqrt{i^2 + ij + j^2}$
Square Lattice	$\frac{P}{\sqrt{(i^2 + j^2)}} \sqrt{\frac{\epsilon_m \epsilon_d}{\epsilon_m + \epsilon_d}}$	$G_{mn} = \frac{2\pi}{a} \sqrt{i^2 + j^2}$

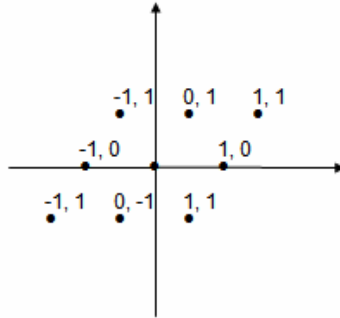


Figure 65: Scattering order for a hexagonal lattice.

Triangular lattices can be produced by Nanosphere Lithography. Using the right processing techniques, Focused Ion Beam Lithography and Nanosphere Lithography can achieve comparable results. Figures 33 and 34 show a similar periodicity using a bitmap image input for the Focused Ion Beam and 1 μm spheres in Nanosphere Lithography. Holes of larger diameter show white light scattering when viewed under a dark field optical microscope, and no peak intensity shifts are noticeable in the raw signal collected by the spectrometer.

The transmission spectrum is not sensitive to the point defects that occur regularly in Nanosphere Lithography,⁸³ but the effects of slip dislocations have not been studied. The features produced by NSL have more broad gold features and exhibit an orange hue from the dark field optical microscope. However, no sharp transmission peaks have been observed.

When photons strike a thin film, if the media on either side of the film are not the same, surface plasmons will be propagating at different speeds. This creates different scattering orders in the transmission spectrum. This also assumes the actual features are symmetric on the top and bottom interface. While Focused Ion Beam may produce symmetric features at the top and bottom interfaces, Nanosphere Lithography creates shadowed regions that can alter the scattering order at the metal/liquid interface. Figure 36 shows the features produced by both methods and the differences between the transmission intensity.

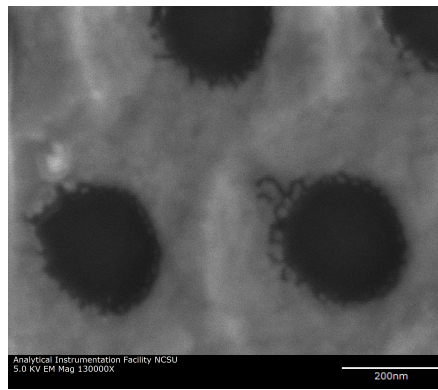


Figure 66: SEM image of Reactive Ion Etched 500 nm spheres (50 sec). Granular nature of gold is evident and the sloping profile is due to shadowing from the spheres in NSL.

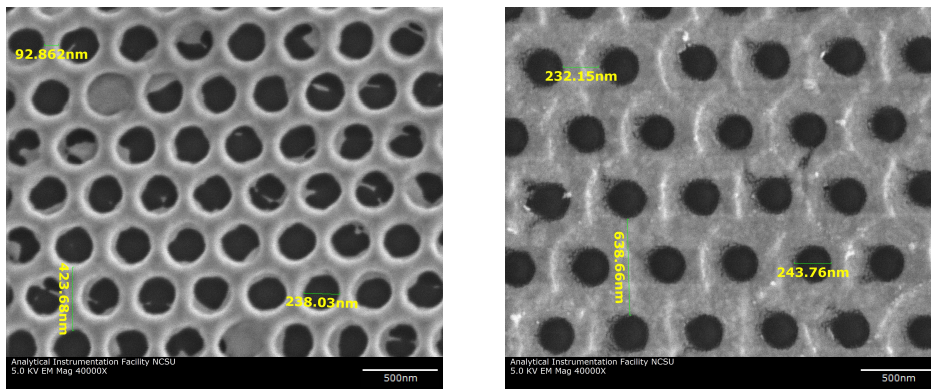


Figure 67: Hexagonal apertures fabricated through A) Focused Ion Beam and B) Nanosphere Lithography.

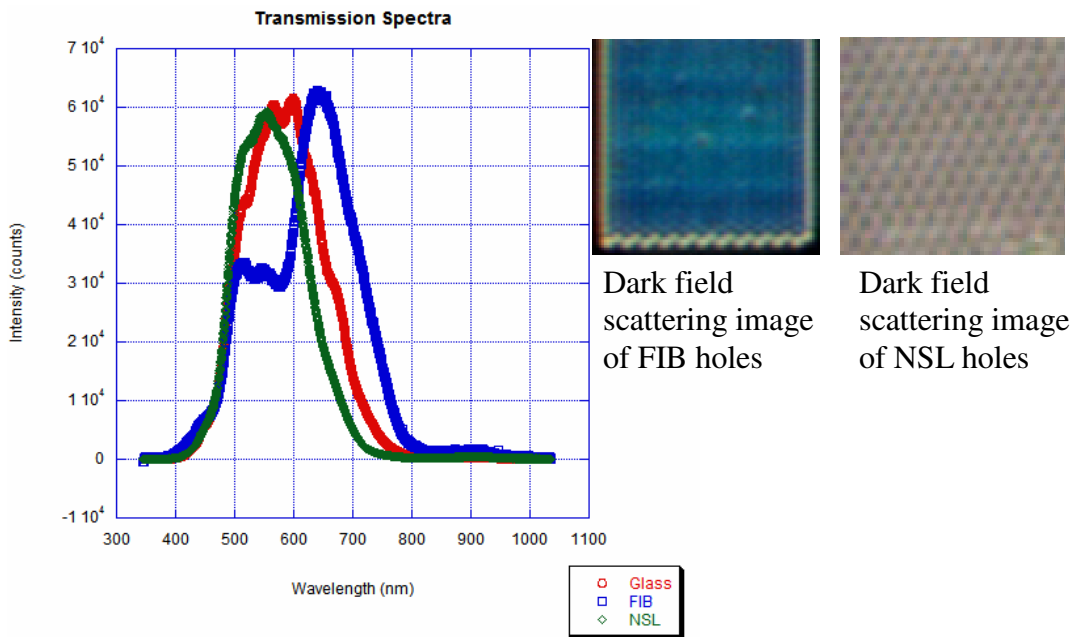


Figure 68: Transmission of light through structures fabricated by FIB and NSL.

Surface Plasmon Polaritons are electromagnetic waves coupled with electron oscillations on the surface of a metal. Because photons are vectorial by nature, the hexagonal arrays show a polarization dependence for a normally incident plane wave. We have obtained preliminary data that validates the polarization dependence for transmission of a linearly polarized white light source (Figure 69). In the hexagonal structures fabricated through NSL, localized plasmons are likely generated, but for certain polarizations there could be propagating surface plasmon modes as well. More data will need to be collected before any conclusions can be made.

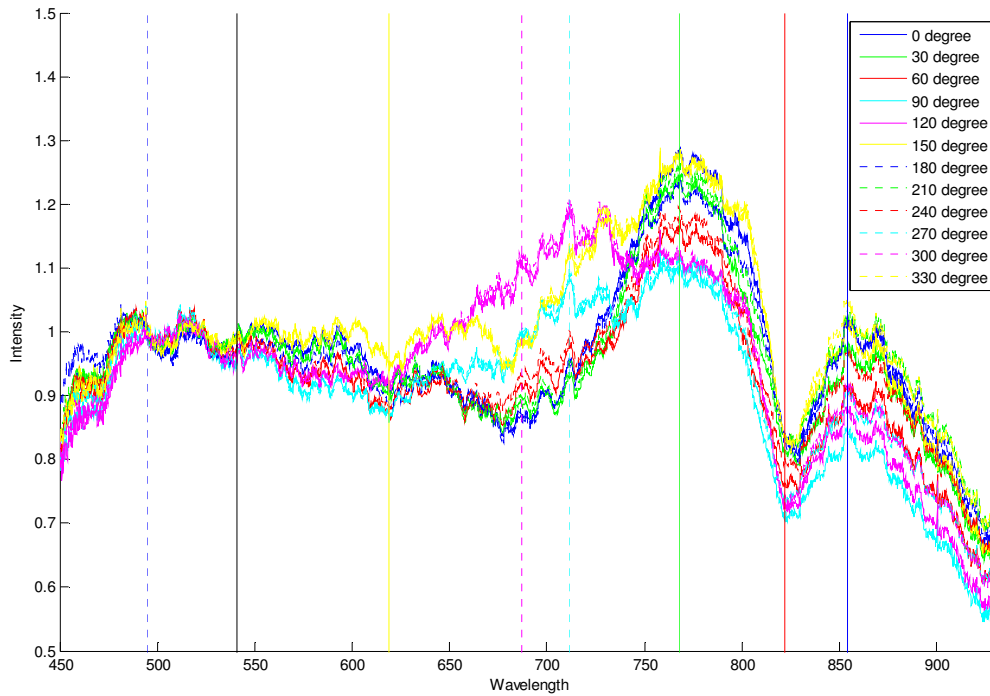


Figure 69: The transmission rate of gold film (150nm) with hexagonal hole-array for different polarization states.

4.4. Sensing and Imaging Potential

Localized Plasmons are sensitive to the surrounding dielectric media. By changing the index of refraction at the surface, the peak wavelength of transmission should shift. Red shifts and blue shifts of the entire spectrum can also occur. Resonant scattering from particles can be observed in transmission mode. For the triangular particles fabricated by Focused Ion Beam Lithography, shown in Figure 29 of section 3.4, changes in the transmission rate and a broadened peak can be observed when immersed in ethanol.

Preliminary data from hexagonal spaced holes fabricated by Focused Ion Beam milled holes show a small red shift in peak transmission for transmission through ethanol, as compared to air. The hexagonal spaced apertures Nanosphere Lithography have not shown the sensitivity demonstrated here by Focused Ion Beam, and this may be due to the surface topology created by the shadowing spheres. This could be interfering with Localized Plasmon modes established at the surface of the periodic structure. It is possible that an anneal step could smooth the films and allow for similar sensing experiments.

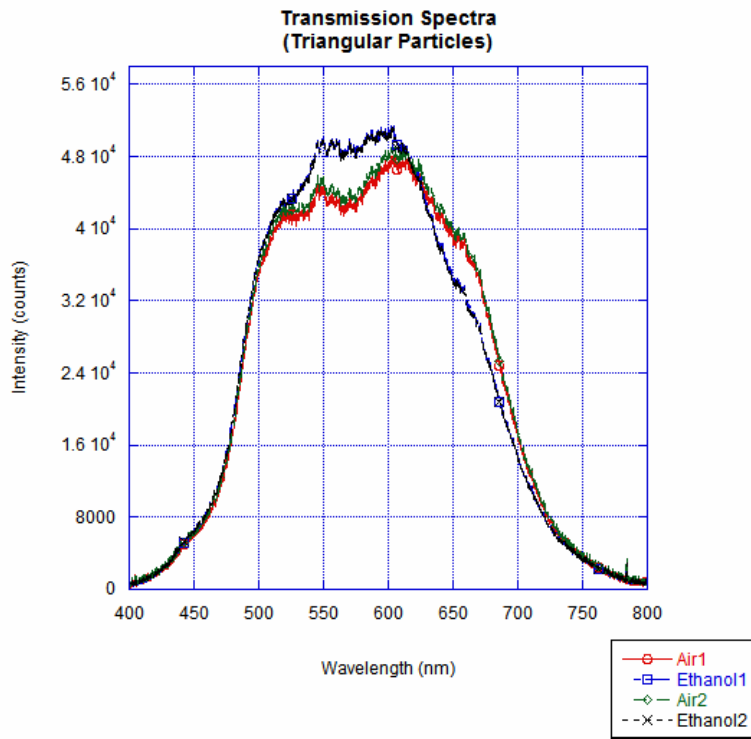


Figure 70: The transmission spectra from periodic triangular particles shows its ability to sense the surrounding dielectric material (Air vs. Ethanol).

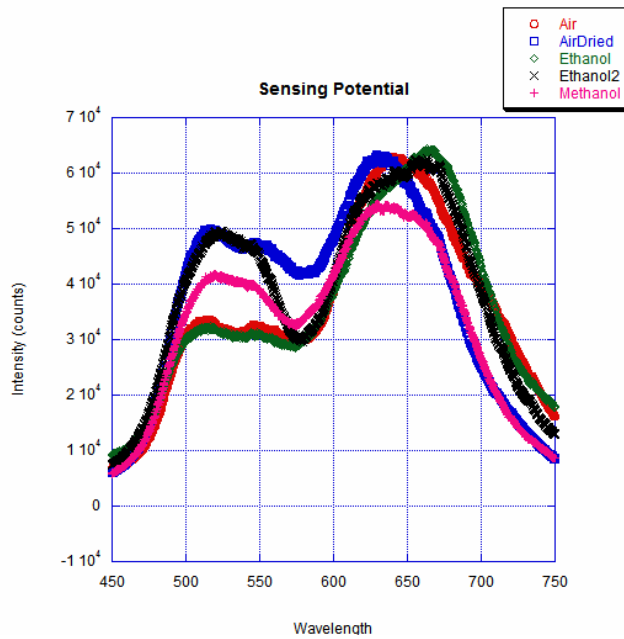


Figure 71: Preliminary data shows small intensity shifts in peak transmission for a variety of liquids.

Chapter 5

Conclusion

5.1. Directed Self-Assembly

Directed Self-Assembly allows for control over the location and size of monolayers and multilayer crystals. A computer controlled stepper motor with image feedback allows the user to adjust the rate of the receding meniscus to compensate for changing evaporation conditions. Brownian motion can cause density shifts in the sphere distribution near the meniscus, which can result in multilayer stacking if the stepper rate is too slow. If the meniscus evaporates or recedes too quickly, the stepper motor can also be driven forward to connect a disjointed monolayer. Defects that arise from randomized self-assembly can be reduced by dragging the droplet over a pre-patterned substrate. The features of the pre-patterned substrate function best when they are between 10 and 20x the diameter of the spheres.

5.2. NSL in producing Sub-wavelength Apertures

Plasmonic structures were fabricated by evaporation of thin gold layers onto transparent substrates. For small scale research studies usually employ Focused Ion Beam has been the primary method of generating periodic patterns. This technique, as previously described, can fabricate structures with unlimited shape and periodicity. Nanosphere Lithography was developed by the Van Duyne group of Northwestern University to pattern hexagonal arrays of triangular particles. By incorporating Reactive Ion Etching of the spheres followed by electron beam deposition of optically thick gold film, a triangular array of apertures can also be made.

Different sphere sizes alter the periodicity of the hexagonal spaced apertures, while etching time can be used to adjust the hole sizes. Sub-wavelength apertures can be applied in biosensing experiments due to the sensitivity of noble metals to the surrounding dielectric media. Adjusting the physical dimensions of the apertures can possibly lead to enhanced light transmission, which could lead to applications in cellular microscopy. Nanosphere Lithography is currently limited

to hexagonal spaced monolayer packing and hexagonal or square lattice multilayer packing. However, apertures fabricated by NSL can find use in a variety of optical devices.

5.3. Suggestions for Future Work

Further reducing packing defects is still possible through either chemical templates or through the use of different spheres. Literature reports have mentioned that the quality of the 2D ordered arrays improved with increasing particle charge, due to enhanced repulsion between particles. This aspect of patterning improvement has not yet been explored by our group at NC State. Experimenting with different sphere surface charges could further reduce packing defects.

The next step towards using these structures in biological applications is to experiment with thiol chemistry bonding of different chemicals to the gold surface. The most frequently studied Self-Assembled Monolayer system is long-chain alkane-thiolates on gold surfaces, due to the simple preparation and stability. Self-Assembled Monolayers on small gold features will likely behave very differently from flat gold surfaces. The nanoparticle surface is highly faceted and hence contains many defect sites such as edges and vertices. Second, due to the curved surface and unlike monolayers on flat gold, SAMs radiate outward from the core. These aspects of surface patterning are important to ensure the viability of using hexagonal periodic structures in cellular biology studies.

Nanosphere Lithography has even found use as a mask for Lysozyme protein deposition in the hexagonal spaces.⁸⁴ This offers promise in using the gold islands and veins as a substrate for assembling chemical and protein scaffolds. After Reactive Ion Etching of the spheres, proteins or chemicals can be adhered to the surface. The spheres can then be removed via ultrasonication.

Chapter 6

References

- [1] Liedberg, B; Nylander, C; Lundstroem, I. Surface plasmon resonance for gas detection and biosensing *Sensors Actuators* **4** (2), 299-304. 1983
- [2] Bethe, H. A. Theory of Diffraction by Small Holes *Physical Review* **66** (7-8), 163-182, 1944.
- [3] Grupp, D. E.; Lezec, H. J.; Thio, T.; Ebbesen, T. W. Beyond the Bethe Limit, *Advanced Materials* **11** (10), 860-862, 1999.
- [4] Ebbesen, T. W.; Lezec, H. J.; Ghaemi, H. F.; Thio, T; Wolff, P. A. Extraordinary optical transmission through subwavelength hole arrays *Nature*, **391**, 667–669, 1998.
- [5] Klar, T. A.; Jakobs, S.; Dyba, M.; Egner, A.; Hell, S. W. Fluorescence Microscopy with diffraction resolution barrier broken by stimulated emission *PNAS* **97** (15), 8206-8210, 2000.
- [6] Stelzer, E. H. K. Beyond the Diffraction Limit? *Nature* **417**, 806-807, 2002.
- [7] Thomson, J. J. Cathode Rays, *Philosophical Magazine*, 44, 293-316, 1897.
- [8] Maxwell, J. C. *Annales de Chimie et de Physique*, 1861.
- [9] Raether, H. Excitation of Plasmons and Interband Transitions by Electrons. Springer Tracts in Modern Physics, 88, 1980.

- [10] Bohm, D; Pines, D. *Physical Review* **82** (5), 625-634, 1951.
- [11] Sauter, F. Physikertag., Dusseldorf 1964.
- [12] Sauter, F. *Z. Physik* **203**, 488, 1967.
- [13] Melnyk, A. R.; Harrison, M. J. *Physical Review B* **2**(4), 835-850, 1970.
- [14] Lindau, I., and P. O. Nilsson. Experimental evidence for excitation of longitudinal plasmons by photons. *Physics Letters A* **31**, 352-3, 1970.
- [15] Lindau, I.; Nilsson, P. O. *Physica Scripta*. **3**, 87-92, 1971.
- [16] Wood, R. W. On Uneven Distribution of Light, *Proc. Phys. Soc. London* **18** 269 275, 1902.
- [17] Matsubara, K.; Kawata, S.; Minami, S. Optical chemical sensor based on surface plasmon measurement. *Applied Optics*, **27**(6), 1160-1163, 1988.
- [18] Ramachandra Rao, C. N.; Kulkarni, G. U.; Thomas, P. J. et al. *Chem. Soc. Rev.* **29**, 27-35, 2000.
- [19] Ventra, M. D.; Evoy, S.; Heflin, J. R. *Introduction to Nanoscale Science and Technology* 2004.
- [20] Lovell, P. A.; El-Aasser, M. S., Eds. *John Wiley & Sons*, New York, 1997.
- [21] Xia, Y.; Gates, G. Yin, Y.; Lu, Y. *Adv. Mater.* **12** (10), 693-713, 2000.
- [22] Qiu, D.; Cosgrove, T.; Howe, A. M. *Macromol. Chem Phys.* **206**, 2233-2238, 2005.
- [23] Fischer, U. C.; Zingsheim, H. P. *J Vac. Sci. Technol.*, **19**, 881-885, 1981.

- [24] Deckman, H. W.; Dunsmuir, J. H. *Appl. Phys. Lett.*, **41**, 377-379, 1982.
- [25] Deckman, H. W.; Dunsmuir, J. H. *J. Vac. Sci. Technol. B*, **1**, 1109-1112, 1983.
- [26] Burmeister, F.; Colloid Monolayers as Versatile Lithographic Masks *Langmuir* **13** (11), 2983-2987, 1997.
- [27] Hulteen, J. C.; Van Duyne, R. P. *J. Vac. Sci. Technol. A* **13**, 1553-1558, 1995.
- [28] Haynes, C. L.; Van Duyne, R. P. *J. Physical Chemistry B* **105**, 5599-611, 2001.
- [29] Haynes, C. L.; Van Duyne, R. P., et al. *J. Phys. Chem. B*, **106** (8), 1898 -1902, 2002.
- [30] Rose J; Baugh D *Mater. Res. Soc. Symp. Proc.*, **832**, 2004 F7.14.1–14.11.
- [31] Cheung, C. L.; Nikolic, R. J.; Reinhardt, C. E., et al. *Nanotechnology* **17**, 1339-1343, 2006.
- [32] Yadong Yin and Younan Xia, *Adv. Mater.* **13** (4), 267-270, 2001.
- [33] Prikulis, J.; Hanarp, P. *Nano Lett.*, **4** (6), 1003-1007, 2004
- [34] Wood, D. M.; Ashcroft, N. W. *Physical Review B* **25** (10), 6255-6274, 1982.
- [35] Parkins, G. R.; Lawrence, W. E.; Christy, R. W. *Physical Review B* **23** (12), 6408-6416, 1981.
- [36] L. V. Lorenz, Lysvevxgelsen i og uden for en af plane lysbolger belyst kugle, K. Dan. Vidensk. Selsk. Forh. **6** (6), 1-62, 1890.
- [37] Mie, G. *Annalen der Physik* **25**, 377-445, 1908.

- [38] Debye, Diss. Munchen *Ann.d Phys.* 30:57-136 1909.
- [39] Kerker, M. Lorenz-Mie Scattering by Spheres: Some Newly recognized phenomena
Aer. Sci. & Tech. **1**, 275-291, 1982.
- [40] Purcell, E. M.; Pennypacker, C. R.; *J. Astrophys.* **186**, 705, 1973.
- [41] Hutter, E.; Fendler, J. H.; *Adv. Mater.* **16** (19), 2004.
- [42] Schatz, G. C.; Young, M. A.; Van Duyne, R. P. *Topics in Applied Physics* **103**,
19-46, 2006.
- [43] Link, S.; El-Sayed, M.A.; Optical Properties and Ultrafast Dynamics of Metallic
Nanocrystals, *Annu. Rev. Phys. Chem.* **54**, 331-366, 2003.
- [44] Blaber, M. G.; Arnold, M. D.; Harris, N., et al. Plasmon absorption in nanospheres:
A comparison of sodium, potassium, aluminum, and gold *Physica B: Condensed
Matter* **394** (2), 184-187, 2007.
- [45] Yguerabide, J.; Ygerabide, E.E. Light-Scattering Submicroscopic Particles as Highly
Fluorescent Analogs and Their Use as Tracer Labels in Clinical and Biological
Applications. *Analytical Biochemistry* **262**, 137-156, 1998.
- [46] Kreibig and Vollmer, Optical Properties of Metal Clusters, *Springer Series in Materials
Science*, **25**, 1995.
- [47] Enoch, S.; Quidant, R.; Badenes, G. *Optics Express* **12** (15), 3422-3427, 2004.
- [48] Fukui, M.; Okamoto, T.; et al. *Proc. of SPIE* **6324** (1), 1-10, 2006.

- [49] Stuart, Douglas A., Chanda Ranjit Yonzon, et. al. Glucose sensing using Near-infrared surface-enhanced raman spectroscopy: Gold surfaces, 10- day stability, and improved accuracy. *Analytical Chemistry* **77**, 4013-9, 2005.
- [50] Forstmann, F; Heine, V. *Physical Review Letters* **24** (25), 1419-1421, 1970.
- [51] Wegner, G. J.; Wark, A. W.; Lee, H. J. Real-Time Surface Plasmon Resonance Imaging Measurements... of Protein Adsorption/Desorption Kinetics *Analytical Chemistry*, **76** (19), 5677-5684, 2004.
- [52] Zhang, X.; Yonzon, C. R.; Young, M. A. et al. *IEE Proc.-Nanobiotechnol.* **152** (6), 195-206, 2005.
- [53] Giebel, K. F.; Bechinger, C.; Herminghaus, S. et al. *Biophysical Journal* **76**, 509-516, 1999.
- [54] Prasad, P. N. Introduction to Biophotonics *John Wiley and Sons, Inc.* p. 317, 2003.
- [55] Pompa, P. P. et al. Metal enhanced fluorescence of colloidal nanocrystals...*Nature Nanotechnology* **1**, 126-130, 2006.
- [56] Rothenhausler, B.; Knoll, W. Surface-plasmon microscopy *Nature* **332**, 615-617, 1988.
- [57] Pawelek, P.D.; Croteau, N.; et al. *Science* **312**, 1399, 2006.
- [58] Kneipp, K.; Haka, A. S.; Kneipp, H. et al. *Applied Spectroscopy* **56** (2), 150-154, 2002.
- [59] Shalaev, V. M.; Kawata, S. Nanophotonics with Surface Plasmons, Elsevier, The Netherlands, 2007.

- [60] Smolyaninov, I. I. Surface Plasmon Toy Model of a Rotating Black Hole, *New J. Phys.*, **5**, 147, 2003.
- [61] H. J. Lezec et al., *Science* **297**, 820, 2002.
- [62] Ferrari, M. Cancer Nanotechnology *Nature: Reviews* **5**, 161-171, 2005.
- [63] Cui, Y.; Qingqiao, W.; Hongkun, P.; Lieber, C. M. *Science*, **293**, 1289-1292, 2001.
- [64] Stern, J. M.; Stanfield, J. et al. Efficacy of Laser-activated Gold Nanoshells in Ablating Prostate Cancer Cells in vitro *Journal of Endourology* **21**(8): 939-943, 2007.
- [65] Lozano, E.; Betson, M.; Braga, V. M. M. Tumor Progression: Small GTPases and loss of cell-cell adhesion *BioEssays*, **25**, 452-463, 2003.
- [66] Gao, D.; Chen, W.; Mulchandani, A. *Applied Physics Letters* **90**, 073901, 2007.
- [67] McCord, M.A.; Rooks, M.J. Handbook of Microlithography, Micromachining and Microfabrication *SPIE & The Institution of Electrical Engineers*, Bellingham, WA. 1997.
- [68] Denkov, N. D.; Velev, O. D.; Kralchesky, P.A., et al. *Langmuir* **8**, 3183-3190, 1992.
- [69] Micheletto, R.; Fukuda, H.; Ohtsu, M. *Langmuir* **11**, 3333-3336, 1995.
- [70] Roberts, G. G. *Advances in Physics* **34** (4), 475-512, 1985.
- [71] Dimitrov, A. S.; Nagayama, K. *Langmuir* **12**, 1303-1311, 1996.
- [72] Lumsdon, S. O., E. W. Kaler, and O. D. Velev. Two-dimensional crystallization of microspheres by a coplanar AC electric field. *Langmuir* **20**, 2108-16, 2004.

- [73] Dushkin, C.D.; Yoshimura, H.; Nagayama, K. Nucleation and Growth of 2-D Colloidal Crystals *Chemical Physics Letters* 204, 455-460, 1993.
- [74] Dimitrov, A. S.; Nagayama, K. Continuous Convective Assembly of Fine Particles...*Langmuir* **1996**, 12, 1303.
- [75] Matsushita, S.; Miwa, T.; Fujishima, A. *Langmuir* **13**, 2582-2584, 1997.
- [76] Barton, E. E.; Celio, H.; Stevenson, K. J. Facile Assembly of Functional Materials using Lithographically Controlled Wetting *Beckman Scholar Research Report*, 1-5, 2005.
- [77] Burmeister, F.; Schafle, C.; Keilhofer, B. et al. *Adv. Mater.* **10**, 495, 1998.
- [78] Degiron, A.; Lezec, J. J.; Barnes, W.L.; Ebbesen, T. W. Effects of hole depth on enhanced light transmission through subwavelength hole arrays. *Appl. Phys. Lett.* **81**, 4327-4329, 2002.
- [79] Cheung, C. L.; Nikoliic, R. J.; Reinhardt, C. E.; Wang, T. F. Fabrication of nanopillars by nanosphere lithography *Nanotechnology* **17**, 1339-1343, 2006.
- [80] Boneberg, J.; Burmeister, F. et al. *Langmuir* **13**, 7080, 1997.
- [81] Maurice, P. A. Applications of AFM in environmental colloid and surface chemistry *Colloids and Surfaces A* **107** (20), 57-75, 1996.
- [82] Wang, Qian-jin; Li, Jia-qi; Huang, Cheng-ping; Zhang, Chao; Zhu, Yong-yuan. Enhanced optical transmission through metal films with rotational-symmetrical hole arrays, *Applied Physics Letters*, **87**, 091105, 2005.

- [83] Thio, T.; Ghaemi, H. F.; Lezec, H. J; Wolff, P. A.; Ebbesen, T. W. Surface Plasmon Enhanced Transmission through hole arrays in Cr films, *J. Opt. Soc. Am. B*, **16**(10), 1743-1748, 1999.
- [84] Cai, Y, Ocko, and B. M. Large-scale fabrication of protein nanoarrays based on nanosphere lithography *Langmuir* **21** 9274-9, 2005.